

# Dynamics of the Bottom Boundary Layer on the Northern California Shelf

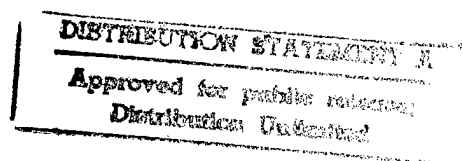
J. H. Trowbridge and S. J. Lentz

Woods Hole Oceanographic Institution

Woods Hole, MA 02543

December 31, 1996

*submitted to: Journal of Physical  
Oceanography*



19970612 038

## Abstract

Time-series measurements of velocity, temperature and conductivity on the northern California shelf during two winter seasons permit an observational test, in vertically integrated form, of a simple set of subinertial momentum and heat balances for the bottom boundary layer, which have resulted from recent theoretical work. These are: (1) an along-isobath momentum equation that reduces to a classical Ekman balance; (2) a cross-isobath momentum equation in which the Ekman balance is modified by a buoyancy force caused by distortion of the isopycnal surfaces within the boundary layer; and (3) a heat balance in which variability of temperature is produced by cross-isobath advection. The measurements confirm the importance of buoyancy in the cross-isobath momentum equation, and, as has recently been predicted theoretically, they indicate that buoyancy is a dominant effect when the boundary layer is thick, which typically occurs during downwelling-favorable flows. An Ekman balance describes subinertial fluctuations in the along-isobath momentum equation with moderate success. The mean along-isobath momentum equation is significantly influenced by a buoyancy force caused by an along-isobath temperature gradient, and along-isobath advection is as important as cross-isobath advection in the heat balance. Thus along-isobath variability of temperature, which has been neglected in most theoretical work, is fundamental to the structure of the velocity field and the evolution of the temperature field.

The most striking feature of the measurements is a persistent cross-isobath mean flow, which is offshore below 20 m above bottom, onshore above 20 m, and uniform above 30 m. The transport produced by this flow, relative to the unsheared flow above 30 m, is much larger than the Ekman transport associated with the mean along-isobath bottom stress. Thus the dominant force producing a mean cross-isobath transport, relative to the unsheared flow above 30 m, is not bottom stress, but must instead be some other mechanism. A likely explanation is a vertically nonuniform along-isobath density gradient, which is poorly resolved by the measurements.

# 1 Introduction

Recent theoretical work on the bottom boundary layer has focused on a problem in which a subinertial, along-isobath flow begins from rest in a stably stratified ocean above a gently sloping, nonconducting sea floor (see the review by Garrett et al. [1993] and the recent articles by Ramsden [1995a, 1995b] and Middleton and Ramsden [1996]). In this problem, the sloping bottom permits the cross-isobath Ekman transport to modify the density field, and the combination of the sloping bottom and the distortion of isopycnal surfaces by mixing and advection produces cross-isobath buoyancy forces that influence the velocity field. The interaction between density and velocity leads to evolution and structure that are profoundly different from the more classical results for a flat bottom. In particular, if the forcing is steady, the models predict evolution toward a steady state in which the along-isobath velocity is brought to zero at the bottom by a frictionless thermal-wind balance that occurs within the boundary layer, so that the bottom stress and cross-isobath Ekman transport vanish and the bottom offers no frictional resistance to the overlying flow.

Although idealized, the recent theoretical work provides a concise set of vertically integrated, subinertial momentum and heat balances that can, at least in principle, be tested observationally. These are: (1) an along-isobath Ekman balance, in which bottom stress is proportional to cross-isobath transport; (2) a cross-isobath momentum equation in which the Ekman balance is modified by a buoyancy force; and (3) a heat balance in which cross-isobath advection produces temporal variability of temperature. These balances represent a simple but oceanographically relevant set of boundary layer processes, and they are fundamental to the existing understanding of the bottom boundary layer and its response to the overlying flow. In particular, the concept of an along-isobath Ekman balance is a cornerstone of geophysical fluid dynamics (e.g., Pedlosky, 1979).

The above balances have not, to our knowledge, been tested observationally. In fact, few oceanic

studies have resolved the structure of the bottom boundary layer. Several researchers have measured velocity and temperature within a few meters of the bottom, without corresponding measurements in the upper part of the boundary layer (see, for example, the reviews by Grant and Madsen [1986], Dyer and Soulsby [1988] and Cacchione and Drake [1990]). Other workers have reported coarsely spaced measurements in the upper part of the boundary layer, without corresponding measurements near the bottom (Kundu, 1976; D'Asaro, 1982a; D'Asaro, 1982b; Lentz and Trowbridge, 1991). Observations with profiling instrumentation have resolved the entire boundary layer, but the durations have been too short for a definitive examination of the sub-inertial dynamics (Mercado and van Leer, 1976; Weatherly and Martin, 1978; Armi and D'Asaro, 1980; Dickey and van Leer, 1984). Recent observations on continental slopes have focused on the structure up to hundreds of meters above bottom, and they have not resolved the much thinner frictional boundary layer in which Ekman dynamics are relevant (Thorpe, 1987; Thorpe et al., 1990; White, 1994). Weatherly's (1972) moored array resolved the bottom boundary layer in the Florida current, but the duration (one week) was too short for a statistically significant examination of subinertial variability, and the analysis was limited primarily to estimating bottom stress, determining the thickness of the logarithmic layer, and documenting Ekman veering. Bird et al. (1982) reported measurements that spanned the bottom boundary layer on the Bermuda Rise for a period of eight months, but the vertical resolution was coarse (four sensors between 0.8 and 62 m above bottom) and the analysis was limited primarily to a qualitative comparison with simulations based on a turbulence closure model.

We report measurements obtained as part of the Sediment Transport Events on Shelves and Slopes (STRESS) program, which resolve the vertical structure of the bottom boundary layer on the northern California shelf during each of two winter seasons. The purpose of the analysis is to test the vertically integrated momentum and heat balances that have resulted from recent theoretical

work. In contrast to previous observations, the STRESS measurements have a duration sufficiently long to examine subinertial variability and they span the boundary layer with vertical resolution sufficiently fine to estimate the terms in the vertically integrated balances. In the following, we first present the theoretical background (Section 2) and describe the measurements and analysis (Section 3). We then present and discuss the results (Sections 4 and 5) and summarize conclusions (Section 6).

## 2 Background

### 2.1 Mathematical model

The mathematical model addresses an idealized configuration in which a turbulent boundary layer above a non-conducting, gently sloping sea floor is overlain by a stratified interior in which turbulent fluxes of momentum and heat are negligible (Figure 1). The coordinate system is defined so that the  $x$ - $y$  plane coincides with the sloping sea floor, with  $x$  cross-isobath,  $y$  along-isobath, and  $z$  perpendicular to the bottom, with  $z = 0$  at the bottom. Time is denoted  $t$ . The time scales of interest and the along-isobath and cross-isobath spatial scales are assumed to be sufficiently large that local and advective accelerations are negligible in comparison with the Coriolis acceleration. The relationship between density  $\rho$  and temperature  $T$  is assumed to be approximately linear; i.e.,  $\rho \simeq \rho_0 - \beta(T - T_0)$ , where  $\rho_0$  is a fixed reference density and  $\beta$  and  $T_0$  are constants. The temperature gradients  $\partial T / \partial x$  and  $\partial T / \partial y$  are assumed to be approximately independent of  $z$  within the boundary layer. This configuration is essentially the same as in the theoretical work reviewed by Garrett et al. (1993), although it is slightly more general in that  $\partial T / \partial y$  is not assumed to be zero.

The dynamics of the boundary layer are described by simplified momentum and heat equations

for a Boussinesq fluid (e.g., Pedlosky, 1979). The  $x$  and  $y$  momentum equations reduce approximately to a balance between Coriolis acceleration, pressure gradient and stress divergence, with an additional gravitational term resulting from the sloping coordinate system. The  $x$  momentum equation is

$$-\rho_0 f v = -\frac{\partial p}{\partial x} + \frac{\partial \tau_{zx}}{\partial z} - \alpha g \rho, \quad (1)$$

and the  $y$  momentum equation is

$$\rho_0 f u = -\frac{\partial p}{\partial y} + \frac{\partial \tau_{zy}}{\partial z}. \quad (2)$$

The  $z$  momentum equation is approximately hydrostatic:

$$0 = -\frac{\partial p}{\partial z} - \rho g, \quad (3)$$

and the heat equation reduces approximately to a balance between time dependence, cross-isobath and along-isobath advection, and vertical mixing:

$$\frac{\partial T}{\partial t} + u \frac{\partial T}{\partial x} + v \frac{\partial T}{\partial y} = \frac{\partial \phi}{\partial z}. \quad (4)$$

Here  $g$  is gravitational acceleration,  $f$  is the Coriolis parameter,  $\alpha$  is the small bottom slope,  $(u, v, w)$  is the velocity vector,  $p$  is pressure,  $\tau_{zx}$  and  $\tau_{zy}$  are components of the stress tensor,  $\phi$  represents turbulent flux of temperature, and  $T$ ,  $\rho$  and  $\rho_0$  are respectively temperature, density and a fixed reference density, as before.

In (4), the term  $w \partial T / \partial z$  has been neglected without obvious justification. In the theoretical work reviewed by Garrett et al. (1993), this term is identically zero because, by assumption, the velocity is everywhere parallel to the bottom, so that  $w = 0$ . Here we point out that even if  $w$  is not precisely zero,  $w \partial T / \partial z$  is small in comparison with  $u \partial T / \partial x$  within the boundary layer,

provided that the temperature in the boundary layer is relatively well mixed. To see this, note that  $w$  is at most  $O(\alpha u)$ , except in front-like regions with short cross-isobath or along-isobath scales, which are excluded from the analysis. In addition,  $\partial T/\partial x$  is  $O(\alpha \partial T_\infty/\partial z)$ , where  $T_\infty$  is the interior temperature (e.g., Garrett et al., 1993). Thus  $u \partial T/\partial x$  is  $O(\alpha u \partial T_\infty/\partial z)$  while  $w \partial T/\partial z$  is  $O(\alpha u \partial T/\partial z)$ , so that  $w \partial T/\partial z \ll u \partial T/\partial x$  provided that  $\partial T/\partial z \ll \partial T_\infty/\partial z$ . Above the boundary layer, where the temperature is not well mixed, neglect of  $w \partial T/\partial z$  is not necessarily justified.

Neglect of temporal accelerations in (1) and (2) is a conspicuous omission, particularly in (2), because shelf measurements typically indicate that  $\partial v/\partial t$  is comparable to  $fu$  for subinertial fluctuations (e.g., Allen, 1980). Neglect of temporal accelerations is, however, an acceptable approximation in the present analysis. Because a proper treatment of temporal acceleration is complicated, the justification is postponed until the discussion (Section 5.3).

## 2.2 Vertically integrated momentum balances

To obtain a set of vertically integrated balances, it is convenient to define  $z = \delta$  to be a position just above the turbulent boundary layer, where turbulent fluxes of heat and momentum are negligible. The quantity  $\delta$  varies with time as the turbulent boundary layer thickens and thins.

Begin by differentiating (1) and (2) with respect to  $z$ , substituting the linear relationship between  $\rho$  and  $T$ , and using (3) to eliminate  $p$ . The result is a pair of equations describing the  $z$  derivatives of  $u$  and  $v$ :

$$-\rho_0 f \frac{\partial v}{\partial z} = -\beta g \left( \frac{\partial T}{\partial x} - \alpha \frac{\partial T}{\partial z} \right) + \frac{\partial^2 \tau_{zx}}{\partial z^2}, \quad (5)$$

and

$$\rho_0 f \frac{\partial u}{\partial z} = -\beta g \frac{\partial T}{\partial y} + \frac{\partial^2 \tau_{zy}}{\partial z^2}. \quad (6)$$

Note that the terms involving temperature in (5) and (6) represent the familiar effect of thermal

wind, expressed in a coordinate system in which the  $x$  axis is inclined at a small angle with respect to horizontal.

Next, integrate (5) and (6) from an arbitrary value of  $z$  to  $z = \delta$ , where  $\partial\tau_{zx}/\partial z$  and  $\partial\tau_{zy}/\partial z$  are zero. The resulting expressions are

$$-\rho_0 f(v - v_\delta) = \beta g \int_z^\delta \left( \frac{\partial T}{\partial x} - \alpha \frac{\partial T}{\partial z'} \right) dz' + \frac{\partial \tau_{zx}}{\partial z}, \quad (7)$$

and

$$\rho_0 f(u - u_\delta) = \beta g \int_z^\delta \frac{\partial T}{\partial y} dz' + \frac{\partial \tau_{zy}}{\partial z}, \quad (8)$$

where subscript  $\delta$  denotes evaluation at  $z = \delta$  and  $z'$  is a dummy variable of integration. Equations (7) and (8) are a restatement of (1) and (2), with quantities involving  $p$  and  $\rho$  expressed in terms of  $u_\delta$ ,  $v_\delta$  and  $T$ .

By integrating (7) and (8) from  $z = 0$  to  $z = \delta$ , one obtains a pair of vertically integrated momentum balances:

$$-\rho_0 f \int_0^\delta (v - v_\delta) dz = \beta g \left[ \frac{\delta^2}{2} \frac{\partial T}{\partial x} + \alpha \int_0^\delta (T - T_\delta) dz \right] - \tau_{bx}, \quad (9)$$

and

$$\rho_0 f \int_0^\delta (u - u_\delta) dz = \beta g \frac{\delta^2}{2} \frac{\partial T}{\partial y} - \tau_{by}, \quad (10)$$

where  $\tau_{bx}$  and  $\tau_{by}$  are the  $x$  and  $y$  components of the bottom stress. The first and last terms in (9) and (10) represent the classical Ekman balance. The terms involving temperature represent buoyancy forces that result from non-horizontal isopycnal surfaces. In the special case in which  $\partial T/\partial y$  is zero, (9) and (10) are consistent with the dynamics in the theoretical work reviewed by Garrett et al. (1993), and they are identical to the expressions used in the vertically integrated



model developed by Trowbridge and Lentz (1991).

### 2.3 Vertically integrated heat balance

A simple form of the vertically integrated heat balance can be obtained by integrating (4) from  $z = 0$  to  $z = \delta$  and applying the condition  $\phi = 0$  at the non-conducting sea floor and in the frictionless interior. The result is

$$\int_0^\delta \frac{\partial T}{\partial t} dz = -\frac{\partial T}{\partial x} \int_0^\delta u dz - \frac{\partial T}{\partial y} \int_0^\delta v dz. \quad (11)$$

The term on the left side of (11) is the vertically integrated temporal variability of temperature within the boundary layer. The terms on the right side represent the effects of cross-isobath and along-isobath advection, respectively. Like (9) and (10), (11) is consistent with the theoretical work reviewed by Garrett et al. (1993) in the special case in which  $\partial T / \partial y$  is zero.

A more dynamically relevant form of the heat balance involves the temperature anomaly  $T - T_\delta$ , because this quantity appears in the buoyancy force in (9) and because it is related to stratification, which influences vertical mixing. Because a heat balance involving  $T - T_\delta$  is substantially more complicated than (11) and requires special treatment, we postpone consideration of this balance until Section 5.

## 3 Methods

### 3.1 Measurements

The STRESS observations (Fredericks et al., 1993; Trowbridge and Nowell, 1994) occurred on the northern California shelf (Figure 2) in approximately the same location as the Coastal Ocean Dynamics Experiment (CODE; see Beardsley and Lentz, 1987). The shelf in the STRESS region

consists of a narrow, steeply sloping inner portion, between the coast and the 70-m isobath, and a broader, gently sloping outer portion, between the 70-m isobath and the shelf break, at a depth of approximately 150 m. The primary site, denoted C3, was at a depth of approximately 90 m. A secondary site on the same isobath, denoted C3', was displaced from C3 by approximately 5 km to the southeast. An additional secondary site, denoted C4, was at a depth of approximately 130 m, approximately 8 km offshore of C3. We use a coordinate system in which the  $y$  axis is positive toward a bearing of  $317^\circ$  relative to true north, which coincides with the isobath orientation at C3, and the  $x$  axis is positive toward a bearing of  $47^\circ$ . The topography near C3 has well defined cross-isobath and along-isobath directions, and our results are not sensitive to small changes in the orientation of the coordinate system.

During 1988–89 (STRESS-1), A. J. Williams, of the Woods Hole Oceanographic Institution, deployed a bottom tripod at C3, and B. Butman, of the U. S. Geological Survey, deployed subsurface moorings at C3 and C3' (Figure 3). The tripod supported six BASS acoustic current meters and eight temperature sensors between heights of 0.2 and 6 m above bottom. The subsurface mooring at C3 supported five vector averaging current meters (VACMs), which record velocity and temperature, at heights between 6 and 30 m, and the subsurface mooring at C3' supported VACMs at 6 and 18 m above bottom. Three of the VACMs at C3 were fitted with temperature–conductivity sensors and optical transmissometers, and both VACMs at C3' were fitted with optical transmissometers. The bottom tripod was within 300 m of the subsurface mooring at C3. The tripod and moorings were on site from 6 December 1988 to 24 January 1989 (STRESS-1a) and from 26 January 1989 to 27 February 1989 (STRESS-1b). All of the instrumentation functioned satisfactorily during both of these periods.

STRESS-1 coincided with the Surface Mixed Layer Experiment (SMILE; see Alessi et al. [1991] and Dever and Lentz [1994]). As part of SMILE, S. J. Lentz and R. C. Beardsley, of the Woods

Hole Oceanographic Institution, deployed a surface mooring at C3. This mooring supported vector measuring current meters (VMCMs), which record velocity and temperature, between a depth of 50 m and the water surface. We use the SMILE measurements briefly (Section 4.1) to illustrate the qualitative structure above the STRESS array.

During 1990–91 (STRESS–2), A. J. Williams deployed bottom tripods and B. Butman deployed subsurface moorings at both C3 and C4 (Figure 3). At each site, the tripod was within 600 m of the mooring. Each tripod supported BASS current meters and temperature sensors between heights of 0.1 and 6 m above bottom. The mooring at C3 supported an array of VACMs fitted with temperature–conductivity sensors and transmissometers, as well as an array of temperature–conductivity sensors. The mooring at C4 supported a VACM, an array of VACMs fitted with temperature–conductivity sensors and transmissometers, a temperature–conductivity sensor, and an array of temperature sensors. Both tripods and both moorings were on site and successfully collecting data from 12 January 1991 to 8 March 1991. Two of the BASS sensors at each site, one of the VACM velocity sensors at C3, and one of the VACM conductivity sensors at C3 malfunctioned (Figure 3).

All of the STRESS instruments obtained measurements essentially continuously but recorded at a number of different rates. In the analysis, we use measurements that have been averaged and resampled to produce time series of hourly averaged values.

### 3.2 Estimation of the terms in the vertically integrated balances

The STRESS measurements provide hourly averaged time series of  $u$ ,  $v$  and  $T$  with relatively fine vertical resolution at C3 and coarser resolution at C3' and C4. To estimate the terms in the vertically integrated balances, we use the measurements at C3 to evaluate quantities involving vertical structure, and we use the measurements at C3' and C4 to provide information about cross–

isobath and along-isobath gradients. To focus on sub-inertial dynamics, we first estimate the terms in the vertically integrated balances by using the hourly averaged data, and we then apply filter pl64 (e.g., Limeburner, 1985), which leaves the energetic subinertial fluctuations nearly unattenuated, while effectively removing the energetic tidal and near-inertial fluctuations (Section 4.1).

Some aspects of this procedure are straightforward. Appropriate values of  $\rho_0$ ,  $f$  and  $\alpha$  are  $1000 \text{ kg m}^{-3}$ ,  $9.1 \times 10^{-5} \text{ s}^{-1}$ , and 0.005, respectively (Figure 2). To determine  $\beta$  we use the best-fit values obtained from the temperature-conductivity measurements, which are  $0.35 \text{ kg m}^{-3} \text{ deg}^{-1} \text{ C}$  for STRESS-1 and  $0.29 \text{ kg m}^{-3} \text{ deg}^{-1} \text{ C}$  for STRESS-2 (Figure 4). To put the velocity and temperature measurements at C3 on a common grid suitable for evaluating vertical integrals, we use the heights of the functioning current sensors as nodes. For nodes at which temperature measurements were not obtained, we assign a temperature record by interpolating between the nearest adjacent temperature measurements. This operation results in a grid of eleven nodes for STRESS-1 and eight nodes for STRESS-2. We use a midpoint rule to estimate integrals with respect to  $z$  and centered differences to estimate time derivatives.

To determine  $\delta$ , we assume that the turbulent boundary layer coincides with the bottom mixed layer. We therefore set  $\delta$  equal to the height of the lowest sensor above the mixed layer, except in the relatively rare occasions when the mixed layer extends to the top of the STRESS array, when we set  $\delta$  equal to the height of the top-most sensor. We estimate mixed-layer thickness by using the procedure described by Lentz and Trowbridge (1991), in which the mixed layer is defined to extend to the highest sensor at which the local temperature is within  $\Delta T$  of the bottom-most temperature, where  $\Delta T$  is an estimate of the uncertainty in the temperature measurements. Here we use  $\Delta T = 0.05^\circ \text{ C}$ , as in Lentz and Trowbridge (1991). Use of mixed-layer thickness to estimate the thickness of the turbulent boundary layer is debatable, because some measurements of turbulence energy dissipation indicate that the two layers do not always coincide (Dewey et al.,

1988). Use of mixed-layer thickness is simple, however, and it is necessary in our case because we have no measurements of turbulence statistics. For the most part, estimates of mixed-layer height are below the height of the top-most sensor (Section 4.2, Figures 12 and 13), so that the measurements resolve the entire mixed layer. Exceptions occur primarily during the first half of STRESS-2 (Section 4.2, Figure 13), when the mixed layer reached the top sensor during a number of events, so that the top of the mixed layer may in fact have been above the top of the measurement array.

Direct estimation of  $\partial T/\partial x$  is possible for STRESS-2 but not for STRESS-1. To obtain a time series of  $\partial T/\partial x$  during STRESS-2, we use the mean of the estimates at nine heights between 0.19 and 19 m based on temperature differences between C3 and C4. The resulting time series of  $\partial T/\partial x$  has a mean of  $0.087^\circ \text{ C per km}$  and a standard deviation of  $0.045^\circ \text{ C per km}$ . The time series of  $\partial T/\partial x$  at the different heights are remarkably consistent (temporal means and standard deviations vary by less than 10% at the different heights and the squared correlation coefficient  $r^2$  is greater than 0.67 for all pairs of estimates). This consistency justifies the assumption (Section 2) that  $\partial T/\partial x$  is independent of  $z$ . To estimate  $\partial T/\partial x$  during STRESS-1, we use a fixed value equal to the mean of the time series obtained during STRESS-2. Although crude, this procedure captures the dominant feature of the bottom temperature field, which is the offshore cooling associated with increasing depth. The STRESS-1 results are insensitive to the precise value of  $\partial T/\partial x$  that we use, and the STRESS-2 results are changed only slightly if we use a fixed value of  $\partial T/\partial x$  rather than the measured time series.

Direct estimation of  $\partial T/\partial y$  is possible for STRESS-1 but not for STRESS-2. To determine  $\partial T/\partial y$  during STRESS-1, we use the mean of the estimates at two heights (6 and 18 m) based on temperature differences between C3 and C3'. The resulting time series of  $\partial T/\partial y$  has a mean of  $-0.015^\circ \text{ C per km}$  and a standard deviation of  $0.020^\circ \text{ C per km}$ . The time series of  $\partial T/\partial y$  at the two

heights are only moderately well correlated ( $r^2 = 0.37$ ), but they have the same dominant features, which are a roughly constant negative value with brief periods of positive values. To estimate  $\partial T/\partial y$  during STRESS-2, we use a fixed value equal to the mean of the time series obtained during STRESS-1. This approach is probably inaccurate, since the standard deviation of  $\partial T/\partial y$  during STRESS-1 is larger than the mean, and since the STRESS-1 results for the heat balance change significantly if we use a fixed value of  $\partial T/\partial y$  instead of the measured time series. However, use of a fixed, representative value at least permits us to evaluate the importance of  $\partial T/\partial y$  during STRESS-2.

To estimate bottom stress, we use the log-profile method (e.g., Sternberg, 1968), which is based on the standard unstratified wall-layer model (e.g., Monin and Yaglom, 1971), in which the flow speed varies with  $z$  according to

$$\sqrt{u^2 + v^2} = \frac{u_*}{\kappa} \ln(z) - \frac{u_*}{\kappa} \ln(z_0), \quad (12)$$

and the flow coincides in direction with the bottom stress. Here  $u_*$  is the shear velocity,  $\kappa$  is von Karman's empirical constant, approximately equal to 0.40, and  $z_0$  is the bottom roughness length. To apply the method, one fits velocity measurements to (12), using  $u_*/\kappa$  and  $(u_*/\kappa) \ln(z_0)$  as free parameters, and then determines the magnitude of the bottom stress from the definition  $|\vec{\tau}_b| = \rho_0 u_*^2$ . Here we fit velocity measurements obtained by the bottom three functioning BASS sensors to (12), and we assume that the bottom stress coincides in direction with the velocity averaged over the bottom three sensors. We use three sensors because the logarithmic model applies only at small heights and because three is the minimum number that permits an assessment of the accuracy of the stress estimates based on discrepancies in the model fits. In addition, the lowest complex empirical orthogonal function (EOF; see, for example Davis [1976]; here based on the complex

velocity  $u + iv$ ), which accounts for more than 85% of the variance in the hourly velocity data from the entire current meter array, indicates that while the speed profiles are logarithmic throughout the BASS array, the direction is vertically uniform (particularly during STRESS-1) only at the lowest three sensors, with subtle but consistent changes in direction at the fourth sensor and above. Thus the model (12), which implies a logarithmic speed profile and a vertically uniform direction, appears to apply only at the bottom three sensors. The relationship between shear velocity and flow speed that results from the log-profile estimates is roughly consistent with a quadratic drag law based on  $z_0 = 0.01$  m (Figure 5), which corresponds to a drag coefficient  $c_d = |\vec{\tau}_b| / [\rho_0(u^2 + v^2)]$  of  $7.5 \times 10^{-3}$  at  $z = 1$  m.

Log-profile estimates of bottom stress are uncertain because of uncertainties in current measurements and because of shortcomings in the logarithmic model caused, for example, by distortions of the near-bottom velocity produced by acceleration (Soulsby and Dyer, 1981) and stratification due to temperature or suspended sediment (e.g., Monin and Yaglom, 1971). To quantify the effect of errors in current measurements in a simple way, assume for the moment that the model (12) is correct, that errors in current measurements have a Gaussian probability distribution, and that the standard deviation of measurement errors is equal to the standard deviation of the ensemble of all residuals from fits of (12) to the hourly averaged velocity measurements from the bottom three BASS sensors, which is 0.0014 m/s for STRESS-1 and 0.0030 m/s for STRESS-2. Given these assumptions, the 95% confidence intervals for estimates of  $u_*$  are  $\pm 0.001$  m/s for STRESS-1 and  $\pm 0.002$  m/s for STRESS-2, indicating uncertainties in stress estimates that are much smaller than the stresses themselves (Figure 5). Our opinion is that uncertainties in  $u_*$  estimates are in fact substantially larger than  $\pm 0.001$  or  $\pm 0.002$  m/s, and that they are caused primarily by shortcomings in the logarithmic model. However, calculations of the effect of flow acceleration based on the model of Soulsby and Dyer (1981), the effect of stratification due to temperature based on an approach

similar to that recently proposed by Friedrichs and Wright (1997), and the effect of stratification due to suspended sediment based on the model developed by Glenn and Grant (1987) indicate that these effects were, for the most part, <sup>appreciable</sup> ~~important~~ only when the bottom stress was weak, so that they are not important for the present purposes. More importantly, with a single exception (Section 5.1), failures to close the vertically integrated momentum balances did not occur during periods in which any of these effects appeared to be large.

## 4 Results

### 4.1 Qualitative temporal variability and vertical structure

Before proceeding to the vertically integrated balances, a brief examination of temporal variability and vertical structure provides a useful qualitative characterization of the observations. Here we present rotary spectra, filtered time series, vertical profiles of statistics, and estimates of gradient Richardson number.

Rotary spectra indicate that velocity fluctuations occurred predominantly in a subinertial band (absolute value of frequency less than approximately 0.5 cpd), a diurnal band, a near-inertial band, and a semidiurnal band (Figure 6). Diurnal and semidiurnal fluctuations had predominantly clockwise polarization, corresponding to negative frequencies in Figure 6, while subinertial currents were primarily along-isobath and therefore had no particular polarization. During STRESS-1, approximately 55% of the velocity variance at the top-most sensor was subinertial, and approximately 35% occurred in the combination of diurnal, semidiurnal and near-inertial bands. In contrast, approximately 85% of the variance at the top-most sensor during STRESS-2 was subinertial. During both STRESS-1 and STRESS-2, fluctuations in bottom stress were predominantly subinertial (Figure 7).



Time series of filtered (i.e., subinertial) along-isobath velocity indicate energetic fluctuations with time scales of several days, during which the flow was predominantly poleward with brief periods of equatorward flow (Figures 8a and 9a). Time series of filtered temperature (Figures 8b and 9b) indicate long periods with strong stratification and other periods when temperature throughout the measurement array was well mixed. The qualitative variability of temperature is generally consistent with a simple model based on the first two terms in (11), in which poleward flow, corresponding to downwelling Ekman transport, produces warming, and equatorward flow, corresponding to upwelling Ekman transport, produces rapid cooling. However, there are obvious exceptions to this simple view (e.g., day 40 during STRESS-1). Thick mixed layers generally correspond to periods of strong poleward flow, as reported by Lentz and Trowbridge (1991).

Statistics of velocity and temperature provide a useful means of illustrating vertical structure. The mean cross-isobath velocity for both STRESS-1 and STRESS-2 is offshore near the bottom and onshore above approximately 20 m above bottom, with a uniform structure at heights above 30 m (Figure 10a). The magnitude and structure of the cross-isobath mean flow are remarkably consistent, especially considering the small magnitude and the fact that three different sensors (BASS, VACM and VMCM) produced the measurements. The mean along-isobath flow is poleward at all sensors, with a magnitude generally much larger than that of the cross-isobath mean flow (Figure 10b). The standard deviations of filtered along-isobath and cross-isobath velocities are comparable to the means (i.e., 0.01 to 0.03 m/s for  $u$  and 0.10 to 0.15 m/s for  $v$ ). The lowest complex EOF (based on the complex velocity  $u + iv$ ), which accounts for more than 93% of the variance in the filtered velocity fields, indicates a vertical structure in which the magnitude (Figure 10c) is strongly sheared near the bottom and the orientation (Figure 10d) is consistent in both magnitude and sense with simple models of the unstratified turbulent Ekman layer (e.g., Ellison, 1956). The mean temperature profiles indicate similar stable stratification during STRESS-1 and STRESS-

2, although temperatures were larger during STRESS-2 (Figure 10e). Fluctuations in filtered temperature have a standard deviation of roughly  $0.5^{\circ}\text{C}$ , and the lowest EOF of filtered temperature fluctuations, which accounts for more than 95% of the variance in the filtered temperature fields, indicates relatively large fluctuations near the bottom during STRESS-1 and a nearly uniform vertical structure during STRESS-2 (Figure 10f).

Calculations of gradient Richardson number  $Ri$ , based on the hourly velocity and temperature measurements and defined by  $Ri = \beta g(\partial T/\partial z)/[(\partial u/\partial z)^2 + (\partial v/\partial z)^2]$ , provide a qualitative indication of the likely importance of stable stratification in suppressing vertical mixing. Histograms of  $Ri$  based on finite difference calculations for both STRESS-1 and STRESS-2 indicate values generally well below the critical value of  $1/4$  indicated by linear theory for onset of instability (Miles, 1961; Howard, 1961) within the bottom two meters, and values generally greater than  $1/4$ , with rare excursions below  $1/4$ , at heights above roughly ten meters (Figure 11). Between heights of one and ten meters, the modal value of  $Ri$  gradually increases, and above fifteen meters the distribution of  $Ri$  is approximately independent of height. These calculations support the use of the unstratified wall layer model (12) to estimate bottom stress based on measurements within roughly two meters of the bottom. The calculations of  $Ri$  indicate that stable stratification probably had a significant effect on vertical mixing at heights greater than a few meters above bottom.

## 4.2 Vertically integrated momentum balances

To examine the vertically integrated momentum balances, we regard the terms on the right sides of (9) and (10) as forcing, and we regard the terms on the left sides as response. One measure of the performance of the vertically integrated momentum balances is the squared correlation coefficient between forcing and response, denoted  $r^2$ . A standard analysis based on Gaussian statistics indicates that for STRESS-1 the critical value of  $r^2$  required to reject the null hypothesis

that  $r^2 = 0$  at the 95% confidence level is approximately 0.21 for (9) and 0.13 for (10). The corresponding critical values of  $r^2$  for STRESS-2 are 0.33 and 0.16, respectively. For both STRESS-1 and STRESS-2, these estimates correspond to a temporal correlation scale (i.e., the ratio of record length to effective number of degrees of freedom) of roughly 4 days for (9) and 2 days for (10).

We first consider the cross-isobath momentum balance. For both STRESS-1 and STRESS-2, the mean and standard deviation of the response,  $-\rho_0 f \int_0^\delta (v - v_\delta) dz$ , are larger than the mean and standard deviation of the forcing term in a simple Ekman balance,  $-\tau_{bx}$ , by a factor of roughly two (Table 1). In addition,  $-\rho_0 f \int_0^\delta (v - v_\delta) dz$  is not significantly correlated with  $-\tau_{bx}$  at the 95% confidence level (Figure 12a and 13a). Thus the measurements do not support a conventional Ekman balance in the cross-isobath momentum equation. In contrast, the standard deviation of the buoyancy force in (9) is comparable to the standard deviation of  $-\rho_0 f \int_0^\delta (v - v_\delta) dz$ , and the mean of the buoyancy term is sufficient, together with the bottom stress, to close the mean cross-isobath momentum balance to within 35% (Table 1), which is remarkably good agreement, considering the magnitude of the fluctuations. In addition, incorporation of the buoyancy term improves the correlation between forcing and response to  $r^2 \simeq 0.55$  (Figures 12b and 13b), which is easily significant at the 95% confidence level. Much of the improvement in  $r^2$  is probably due simply to the fact that both the response and the buoyancy force tend to increase in magnitude as  $\delta$  increases. However, the fact that the forcing captures the mean response and the magnitude of the fluctuations in response indicates that the good agreement in Figures 12b and 13b is physically meaningful, rather than being an artifact of dependence on  $\delta$ . Thus the measurements indicate clearly that buoyancy is an important part of the cross-isobath momentum balance.

For both STRESS-1 and STRESS-2, the buoyancy force in the cross-isobath momentum equation is large when the mixed layer is thick (Figures 12 and 13). In STRESS-1, the buoyancy force is much larger than the along-isobath bottom stress during two brief downwelling events (i.e., events

with offshore bottom stress) centered on days -12 and 40 (Figure 13b). During STRESS-2, the buoyancy force is much larger than the bottom stress during two downwelling events of longer duration, centered on days 25 and 35, and also during a brief upwelling event (i.e., an event with onshore bottom stress) centered on day 50. For the most part, these observations are consistent with theoretical work (e.g., Trowbridge and Lentz, 1991) indicating that mixed layers are thick during downwelling-favorable flows, and that a thick mixed layer produces a large cross-isobath buoyancy force that becomes the dominant effect balancing  $-\rho_0 f \int_0^\delta (v - v_\delta) dz$ .

We next consider the along-isobath momentum balance. In this case, the standard deviation of the response,  $\rho_0 f \int_0^\delta (u - u_\delta) dz$ , is comparable to the forcing term in a simple Ekman balance,  $-\tau_{by}$ , and both are much larger than the standard deviation of the buoyancy term (Table 1). The correlation between forcing and response ( $r^2 \simeq 0.33$ ) is easily significant at the 95% confidence level (Figures 14a and 15a), although it is smaller than the corresponding correlation for the cross-isobath momentum balance. Addition of the buoyancy term produces a marginal and probably statistically insignificant improvement in the correlation between forcing and response only for STRESS-2 (Figures 14b and 15b). The buoyancy term is important in the mean along-isobath momentum balance, since the mean buoyancy force is approximately half of the mean along-isobath bottom stress (Table 1). The mean along-isobath momentum balance closes within 20% for both STRESS-1 and STRESS-2 (Table 1). The presence of a dynamically significant buoyancy force in the along-isobath momentum balance is not consistent with the theoretical work reviewed by Garrett et al. (1993), in which along-isobath variability was assumed to be zero.

It is noteworthy that the comparisons of forcing and response in the momentum balances are dominated by a few large events, particularly in the case of the cross-isobath momentum equation (Figures 12 and 13). Thus the effective number of degrees of freedom is small, in spite of the fact that the record length is much longer than in previous observational studies that resolve the vertical

structure of the bottom boundary layer.

### 4.3 Vertically integrated heat balance

To examine the vertically integrated heat balance, we regard the term on the left side of (11) as response and the terms on the right side as forcing. As in the case of the momentum balances, one measure of the performance of the vertically integrated heat balance is the squared correlation coefficient  $r^2$  between forcing and response. A standard analysis based on Gaussian statistics indicates that for (11) the critical value of  $r^2$  required to reject the null hypothesis that  $r^2 = 0$  at the 95% confidence level is 0.06 for STRESS-1 and 0.07 for STRESS-2. Both of these values correspond to a temporal correlation scale (ratio of record length to effective number of degrees of freedom) of roughly 1 day.

Although statistically significant at the 95% confidence level, the correlation between response and forcing for the heat balance (11) is small if we consider only cross-isobath advection (Figures 16a and 17a). The correlation between forcing and response improves dramatically if we include along-isobath advection (Figures 16b and 17b). The standard deviations of cross-isobath and along-isobath advection are nearly identical, and the mean along-isobath advection is substantially larger than the mean cross-isobath advection (Table 1). As in the momentum balance, the importance of along-isobath advection in the heat balance is not consistent with the theoretical work reviewed by Garrett et al. (1993) in which along-isobath variability was neglected.

Note that the mean heat balance does not close well, particularly for STRESS-2 (Table 1). For both STRESS-1 and STRESS-2, the estimates of the advective terms in the heat balance indicate that, in the mean, the boundary layer should be warming more rapidly than is observed. This discrepancy is likely a result of the fact that the measurements do not resolve  $\partial T/\partial x$  and  $\partial T/\partial y$  particularly well.

## 5 Discussion

### 5.1 Discrepancies in the momentum balances

In STRESS-1, discrepancies in the cross-isobath momentum balance occurred primarily during brief events near day -10 and just before day 40 (Figure 12) and discrepancies in the along-isobath momentum balance occurred during the same periods and also near day 10 (Figure 14). An examination of these periods is instructive.

During day -10, transmissometer records indicate the largest turbidities that were recorded during STRESS-1, apparently because of wave-induced sediment resuspension during a severe storm. Stable stratification by suspended sediment might have influenced the near-bottom flow during this period, resulting in over-estimation of the magnitude of bottom stress by the log-profile method. This idea is consistent with analyses by Gross et al. (1992) and Wiberg et al. (1994) of optical transmission measurements obtained during the STRESS program, which suggest that sediment concentrations were large enough during a few severe storms to influence the near-bottom flow. Also in support of this idea, estimates of stress obtained from a quadratic drag law with a fixed drag coefficient based on  $z_0 = 0.01$  m remove, essentially completely, the discrepancies during this period in both (9) and (10). Use of a quadratic drag law with a fixed drag coefficient does not necessarily improve closure of (9) and (10) during other periods, probably because of real variability in the effective bottom roughness, which is captured by the log-profile method but not by a drag law with a fixed drag coefficient.

In the discrepancy in the along-isobath momentum balance that occurs near day 10 (Figure 14),  $\rho_0 \int_0^\delta (u - u_\delta) dz$  is much smaller than  $-\tau_{by}$ . This discrepancy disappears essentially completely (without introducing a discrepancy in the cross-isobath momentum balance) if we set  $\delta$  equal to the height of the top-most sensor, rather than the sensor just above the mixed layer. This fact

suggests that mixed layer thickness is a poor estimate of boundary layer thickness during this particular event; i.e., that  $\tau_{zy}$  just above the mixed layer is not negligible, as required at  $z = \delta$  in the mathematical model (Section 2.2). These ideas are amplified by an examination of velocity and temperature profiles. The mean temperature profile during day 10 (Figure 18b) indicates a mixed layer with a height of approximately 5 m. Above the mixed layer, there is a thick transition layer between heights of roughly 5 and 20 m above bottom, where the stratification is much larger than the stratification above 20 m. The cross-isobath velocity is nonzero and sheared in the transition layer as well as the mixed layer (Figure 18a). It is likely that turbulent momentum transfer extended above the mixed layer and well into the transition layer during this period, so that mixed-layer height is a poor estimate of boundary layer height. We believe that the vertical structure in Figure 18 is typical of strong upwelling events, but this hypothesis is difficult to test based on the existing observations because strong upwelling events are rare in the STRESS measurements. The vertical structure during the more common strong downwelling events indicates a thick well-mixed layer overlain by a stratified interior, without a transition layer, so that mixed-layer height is probably an accurate estimate of boundary layer height during downwelling.

Dever and Lentz (1994) observed anomalously large horizontal temperature gradients near day 40 in the SMILE measurements, which had more extensive spatial coverage than the STRESS measurements, and they tentatively attributed this behavior to the presence of a mesoscale eddy on the shelf. It is likely that during this period the scales of the density field changed and that our estimates of cross-isobath and along-isobath buoyancy forces, which are crude and involve implicit assumptions about spatial scales, are inaccurate. Failure to estimate buoyancy forces accurately might have caused the discrepancies in the momentum balances that occur near day 40.

While not definitive, the above discussion suggests that shortcomings in our ability to close the momentum balances based on the STRESS-1 measurements result from occasional problems

in estimation of bottom stress, boundary layer thickness, and cross-isobath and along-isobath buoyancy forces. During STRESS-2, failures to close the momentum balances are less event-like (Figures 13 and 15) and not as clearly linked to specific explanations, but similar problems probably occurred. It is noteworthy that our results do not suggest shortcomings in the dynamics represented by (9) and (10), but instead in our ability to estimate the terms in these equations based on the existing measurements.

## 5.2 A balance for temperature anomaly

The heat balance (9) is useful because it permits us to examine the relative importance of cross-isobath and along-isobath advection in determining the vertically integrated variability of temperature within the boundary layer. A more dynamically relevant balance, however, involves the vertically integrated anomaly in temperature within the boundary layer, relative to the temperature in the overlying flow. As noted in Section 2.3, temperature anomaly is more relevant dynamically than temperature because the anomaly  $T - T_\delta$  appears in the buoyancy term in the cross-isobath momentum balance and because it is related to stratification, which influences vertical mixing.

To obtain a vertically integrated balance for temperature anomaly that is sufficiently simple for an observational test, let  $h$  denote a fixed height large enough that  $z = h$  is always above the boundary layer, so that turbulent fluxes of heat and momentum are negligible at  $z = h$ . As in Section 2, we assume that  $w \partial T / \partial z \ll u \partial T / \partial x$  and that  $\partial T / \partial x$  and  $\partial T / \partial y$  are independent of  $z$ . Equation (4) then yields

$$\frac{\partial T_h}{\partial t} + u_h \frac{\partial T}{\partial x} + v_h \frac{\partial T}{\partial y} = 0, \quad (13)$$

where subscript  $h$  denotes evaluation at  $z = h$ . By subtracting (13) from (4), integrating the resulting expression from  $z = 0$  to  $z = h$ , and applying the condition  $\phi = 0$  at both limits, one



obtains

$$\frac{\partial}{\partial t} \int_0^h (T - T_h) dz = -\frac{\partial T}{\partial x} \int_0^h (u - u_h) dz - \frac{\partial T}{\partial y} \int_0^h (v - v_h) dz, \quad (14)$$

which is a vertically integrated balance for the anomaly  $T - T_h$ . The term on the left side is the time derivative of the vertically integrated temperature anomaly, and the terms on the right side represent the effects of cross-isobath and along-isobath advection. Note that in (13) we can change the order of evaluation at  $z = h$  and differentiation with respect to  $t$  because  $h$  is fixed. Similarly, in (14), use of fixed  $h$  permits changing the order of integration with respect to  $z$  and differentiation with respect to  $t$ . Use of the variable height  $z = \delta(t)$  would have resulted in additional terms in (14), which are extremely difficult to evaluate observationally.

Our attempts to close (14) based on the STRESS measurements, with  $h$  fixed at the height of the top-most sensor or any other sensor, fail convincingly. The magnitudes of our estimates of the advective terms in (14) are comparable to that of the time-derivative term, but the means are different and the variability is essentially uncorrelated. The squared correlation coefficient  $r^2$  between the time derivative term and the sum of the advective terms is 0.01 for both STRESS-1 and STRESS-2, which is well below the critical value required to reject the null hypothesis of zero correlation at the 95% confidence level. These results do not change if we neglect one of the advective terms, and they also do not change if we assume that the subinertial momentum balances are exactly correct, so that we can use the right sides of (9) and (10) (with  $\delta$  replaced by  $h$ ) to estimate one or both of  $\int_0^h (u - u_h) dz$  and  $\int_0^h (v - v_h) dz$ . Failure to close (14) is probably a consequence of the fact that the terms in this balance involve only differences in velocity and temperature, which are perhaps not accurately determined by the measurements, and the fact that the advective terms involve  $\partial T / \partial x$  and  $\partial T / \partial y$ , which are not well resolved by the measurements. A related issue is that the assumption of vertically uniform  $\partial T / \partial y$  is probably unrealistic, particularly

above the bottom mixed layer.

### 5.3 Other features of the measurements

One of the most striking features of the observations is the mean cross-isobath velocity profile (Figure 10a), which indicates an unsheared interior above a sheared near-bottom flow with a thickness of approximately 30 m. To discuss this profile, note that in (10) we can replace the variable boundary layer thickness  $\delta(t)$  with the fixed height  $h$  introduced in Section 5.2, here set equal to the height of the top-most sensor in the STRESS array. The mean of the resulting expression is

$$\rho_0 f \int_0^h \overline{(u - u_h)} dz = \beta g \frac{h^2}{2} \frac{\partial \overline{T}}{\partial y} - \overline{\tau}_{by}, \quad (15)$$

where an overbar denotes a mean value. The quantity on the left side of (15) is larger than the stress on the right side by a factor of approximately eight for STRESS-1 and four for STRESS-2 (Table 1), so that stress plays a minor role. Therefore, if we expand our viewpoint from considering only the bottom mixed layer ( $z \leq \delta$ ) to considering the bottom few tens of meters, we find that the dominant forcing producing a mean cross-isobath transport, relative to the overlying unsheared flow, is not bottom stress, as is classically assumed, but must instead be some other mechanism.

The measurements do not indicate clearly what balances the left side of (15). Our estimate of the buoyancy term on the right side (obtained directly only during STRESS-1) is smaller by a factor of 2.4 than the left side (Table 1), so that the balance does not close. This observation is interesting because the mean of the corresponding expression (10) closes quite well for STRESS-1 (Table 1). A significant nonlinear effect does not seem likely because of the relatively long cross-isobath and along-isobath scales of the topography (Figure 2) and because crude estimates of  $v \partial v / \partial y$  based on differences between C3 and C3' (possible only for STRESS-1) suggest that this term makes a contribution much smaller than the left side of (15). Our opinion is that our estimates

of the buoyancy term on the right side of (15) are not particularly accurate, particularly above the boundary layer, where our assumption that  $\partial T/\partial y$  is independent of  $z$  might be particularly unrealistic, and that buoyancy is in fact the dominant effect balancing the left side of (15). This idea is interesting because the buoyancy force must be trapped in the bottom 30 m in order to explain the unsheared cross-isobath velocity above 30 m.

An additional striking feature of the observations is the Ekman-like structure indicated by the most energetic EOF of velocity (Figure 10), which represents all but a small fraction of the variance in the subinertial velocity field. It is natural to ask whether this EOF representation is more consistent with the vertically integrated momentum balances than are the original measurements. We have found that the time series described by the most energetic EOF mode for velocity and most energetic EOF mode for temperature are in substantially worse agreement with (9) and (10) than are the original time series. Thus the velocity and temperature profiles represented by the most energetic EOF modes do not reflect the dynamics represented by the vertically integrated momentum balances.

A brief consideration of temporal acceleration, which was neglected in the vertically integrated momentum balances, is convenient at this point. If one includes temporal acceleration in (1) and (2) and uses Leibniz's rule to interchange the order of integration with respect to  $z$  and differentiation with respect to  $t$  in deriving (7) and (8) from (5) and (6), the result is addition of  $\partial/\partial t \int_0^\delta \rho_0(u - u_\delta) dz + \rho_0 \delta (\partial \delta / \partial t) (\partial u / \partial z)_\delta$  to the left side of (9) and addition of  $\partial/\partial t \int_0^\delta \rho_0(v - v_\delta) dz + \rho_0 \delta (\partial \delta / \partial t) (\partial v / \partial z)_\delta$  to the left side of (10). We have confidence in our ability to estimate  $\partial/\partial t \int_0^\delta (u - u_\delta) dz$  and  $\partial/\partial t \int_0^\delta (v - v_\delta) dz$  with reasonable accuracy based on the STRESS measurements, but we have no confidence in estimates of the terms involving  $\partial \delta / \partial t$ , primarily because these terms are highly nonlinear and because of the coarseness of the STRESS array at heights above 6 m (Figure 3), which makes evaluation of velocity gradients and  $\partial \delta / \partial t$

problematic. Consequently, a quantitative assessment of the importance of temporal acceleration is not possible. A qualitative assessment can be obtained, however, by considering only the quantities  $\partial/\partial t \int_0^\delta \rho_0(u - u_\delta) dz$  and  $\partial/\partial t \int_0^\delta \rho_0(v - v_\delta) dz$ . The means of these quantities are two orders of magnitude smaller than the means of the leading terms in (9) and (10), and their standard deviation are smaller by at least a factor of five than the standard deviations of the leading terms (Table 1). These results indicate that temporal acceleration has only a minor effect on vertically integrated momentum balances for the subinertial flow. This conclusion is not surprising for the cross-isobath momentum balance, since  $\partial u/\partial t \ll fv$  for sub-inertial flows, but it is at first surprising for the along-isobath momentum balance, since  $\partial v/\partial t$  and  $fu$  are comparable. The reason that temporal acceleration is not important in the vertically integrated along-isobath momentum balance is that  $(u - u_\delta)$  and  $(v - v_\delta)$  are comparable, even though  $u \ll v$ , so that  $\partial/\partial t(v - v_\delta) \ll f(u - u_\delta)$  for sub-inertial fluctuations.

## 6 Conclusion

We have presented an observational test of a set of vertically integrated, subinertial balances for momentum and heat in the bottom boundary layer, based on time-series measurements obtained on the northern California shelf during each of two winter seasons. As has recently been predicted theoretically, the measurements indicate clearly that the cross-isobath momentum equation does not reduce simply to a classical Ekman balance, but instead includes a dynamically significant buoyancy force resulting from the distortion of isopycnal surfaces within the boundary layer. Also as predicted theoretically, the cross-isobath buoyancy force is dominant when the boundary layer is thick, which typically occurs during downwelling-favorable flows. Subinertial fluctuations in the along-isobath momentum balance are crudely consistent with an Ekman balance. The mean along-isobath momentum balance is significantly affected by a buoyancy force produced by an

along-isobath temperature gradient, and along-isobath advection is as important as cross-isobath advection in the heat balance.

Two important conclusions result from our work. The first is that a buoyancy force produced by distortion of the isopycnal surfaces within the boundary layer is a significant term in the cross-isobath momentum balance, and that the buoyancy force behaves in approximately the manner predicted by the recent theoretical models. The second conclusion is that along-isobath variability of temperature has an important effect on the bottom boundary layer. The along-isobath temperature gradient influences both the heat balance, where it contributes along-isobath advection, and the mean momentum balance, where it produces an along-isobath buoyancy force that modifies the cross-isobath velocity. Thus along-isobath variability of temperature influences both the evolution of the temperature field and the structure of the velocity field. These effects have been neglected in the theoretical work on the bottom boundary layer that was reviewed by Garrett et al. (1993) and in most numerical simulations of the entire shelf (e.g., Allen et al., 1995; Allen and Newberger, 1996), although they have been included in the theoretical model developed recently by Chapman and Lentz (in press).

An important observation also results from our work. The measurements indicate a mean cross-isobath velocity that is offshore below 20 m above bottom, onshore above 20 m, and uniform above 30 m. The transport produced by this flow, relative to the unsheared flow above 30 m, is larger by a factor of four to eight than the Ekman transport associated with the mean along-isobath bottom stress. Thus the dominant mechanism producing a mean cross-isobath transport, relative to the unsheared flow above 30 m, is not bottom stress, as is classically assumed, but must be some other mechanism. A likely mechanism is a vertically nonuniform along-isobath buoyancy force, which is poorly resolved by the measurements.

## Acknowledgments

The STRESS measurement program was funded by the Geology and Geophysics program of the Office of Naval Research (ONR). The present analysis of the STRESS observations was funded by ONR's Coastal Sciences program under grant N00014-89-J-1074. J. H. Trowbridge's participation in the analysis was also funded in part by ONR's Geology and Geophysics program under grant N00014-94-1-0296. We are grateful for this substantial and consistent financial support. We are also grateful to A. J. Williams and B. Butman for permitting us to use their measurements. This is contribution 9319 from the Woods Hole Oceanographic Institution.

## References

- Allen, J. S. 1980. Models of wind-driven currents on the continental shelf. *Annu. Rev. Fluid Mech.* 12, 389-434.
- Allen, J. S., Newberger, P. A. and Federiuk, J. 1995. Upwelling circulation on the Oregon continental shelf. Part 1: response to idealized forcing. *J. Phys. Oceanogr.* 25, 1843-1866.
- Allen, J. S. and Newberger, P. A. 1996. Downwelling circulation on the Oregon continental shelf. Part 1: response to idealized forcing. *J. Phys. Oceanogr.* 26, 2011-2035.
- Alessi, C. A., Lentz, S. J. and Beardsley, R. C. 1991. Shelf MIXed Layer Experiment (SMILE) Program Description and Coastal and Moored Array Data Report. *Tech. Rep. WHOI-91-39*, Woods Hole Oceanographic Institution, Woods Hole, MA, 211 pp.
- Armi, L. and D'Asaro, E. 1980. Flow structures of the benthic ocean. *J. Geophys. Res.* 85, 469-484.
- Beardsley, R. C. and Lentz, S. J. 1987. The Coastal Ocean Dynamics Experiment collection: an introduction. *J. Geophys. Res.* 92, 1455-1464.
- Bird, A. A., Weatherly, G. L. and Wimbush, M. 1982. A study of the bottom boundary layer over the eastward scarp of the Bermuda Rise. *J. Geophys. Res.* 87, 7941-7954.
- Cacchione, D. A. and Drake, D. E. 1990. Shelf sediment transport. *The Sea*, Vol. 9 (B. Le Mehaute and D. M. Hanes, eds.), pp. 729-774, Wiley.
- Chapman, D. C. and Lentz, S. J. Adjustment of stratified flow over a sloping bottom. *J. Phys. Oceanogr.* (in press).
- D'Asaro, E. 1982a. Velocity structure of the benthic ocean. *J. Phys. Oceanogr.* 12, 313-322.

- D'Asaro, E. 1982b. Absorption of internal waves by the benthic boundary layer. *J. Phys. Oceanogr.* 12, 323-336.
- Davis, R. E. 1976. Predictability of sea surface temperature and sea level pressure anomalies over the north Pacific Ocean. *J. Phys. Oceanogr.* 6, 249-266.
- Dever, E. P. and Lentz, S. J. 1994. Heat and salt balances over the northern California shelf in winter and spring. *J. Geophys. Res.* 99, 16001-16017.
- Dewey, R. K., LeBlond, P. H. and Crawford, W. R. 1988. the turbulent bottom boundary layer and its influence on local dynamics over the continental shelf. *Dyn. Atmos. Oceans* 12, 143-172.
- Dickey, T. D. and van Leer, J. C. 1984. Observations and simulations of a bottom Ekman layer on a continental shelf. *J. Geophys. Res.* 89, 1983-1988.
- Dyer, K. R. and Soulsby, R. L. 1988. Sand transport on the continental shelf. *Ann. Rev. Fluid Mech.* 20, 295-324.
- Ellison, T. H. 1956. Atmospheric turbulence. *Surveys in Mechanics* (G. K. Batchelor and R. M. Davies, eds.), pp. 400-430, Cambridge University Press.
- Fredericks, J. J., Trowbridge, J. H., Williams, A. J., Lentz, S. J., Butman, B. and Gross, T. F. 1993. Fluid mechanical measurements within the bottom boundary layer over the northern California continental shelf during STRESS. *Woods Hole Oceanographic Institution Technical Report*, WHOI-94-04, Woods Hole, MA.
- Friedrichs, C. T. and Wright, L. D. 1997. Sensitivity of bottom stress and bottom roughness estimates to density stratification, Eckernforde Bay, southern Baltic Sea. *J. Geophys. Res.* 102.



- Garrett, C., MacCready, P. and Rhines, P. 1993. Boundary mixing and arrested Ekman layers: rotating stratified flow near a sloping boundary. *Ann. Rev. Fluid Mech.* 25, 291-323.
- Glenn, S. M. and Grant, W. D. 1987. A suspended sediment stratification correction for combined wave and current flows. *J. Geophys. Res.* 92, 8244-8264.
- Grant, W. D. and Madsen, O. S. 1986. The continental shelf bottom boundary layer. *Ann. Rev. Fluid Mech.* 18, 265-305.
- Gross, T. F., Isley, A. E. and Sherwood, C. R. 1992. Estimation of stress and bed roughness during storms on the northern California shelf. *Cont. Shelf Res.* 12, 389-413.
- Howard, L. N. 1961. Note on a paper of John W. Miles. *J. Fluid Mech.* 10, 509-512.
- Kundu, P. K. 1976. Ekman veering observed near the ocean bottom. *J. Phys. Oceanogr.* 6, 238-242.
- Lentz, S. J. and Trowbridge, J. H. 1991. The bottom boundary layer over the northern California shelf. *J. Phys. Oceanogr.* 21, 1186-1201.
- Limeburner, R. 1985. CODE-2: Moored array and large-scale data report. *Technical Rep. WHOI-85-35*, Woods Hole Oceanographic Institution, Woods Hole, MA, 234 pp.
- Mercado, A. and van Leer, J. 1976. Near bottom velocity and temperature profiles observed by cyclosonde. *Geophys. Res. Lett.* 3, 633-636.
- Middleton, J. F. and Ramsden, D. 1996. The evolution of the bottom boundary layer on the sloping continental shelf: a numerical study. *J. Geophys. Res.* (in press).
- Miles, J. W. 1961. On the stability of heterogeneous shear flows. *J. Fluid Mech.* 10, 496-508.

Monin, A. S. and Yaglom, A. M. 1971. *Statistical Fluid Mechanics*. MIT Press.

Pedlosky, J. 1979. *Geophysical Fluid Dynamics*. Springer-Verlag.

Ramsden, D. 1995a. Response of an oceanic bottom boundary layer on a slope to interior flow, part 1: time-independent interior flow. *J. Phys. Oceanogr.* 25, 1672-1687.

Ramsden, D. 1995b. Response of an oceanic bottom boundary layer on a slope to interior flow, part 2: time-dependent interior flow. *J. Phys. Oceanogr.* 25, 1688-1695.

Soulsby, R. L. and Dyer, K. R. 1981. The form of the near-bed velocity profile in a tidally accelerating flow. *J. Geophys. Res.* 86, 8067-8074.

Sternberg, R. W. 1968. Friction factors in tidal channels with differing bed roughness. *Mar. Geol.* 6, 243-260.

Thorpe, S. A. 1987. Current and temperature variability on the continental slope. *Phil. Trans. R. Soc. London Ser. A.* 331, 183-194.

Thorpe, S. A., Hall, P. and White, M. 1990. The variability of mixing on the continental slope *Phil. Trans. R. Soc. London Ser. A.* 331, 183-194.

Trowbridge, J. H. and Lentz, S. J. 1991. Asymmetric behavior of an oceanic boundary layer above a sloping bottom. *J. Phys. Oceanogr.* 21, 1171-1185.

Trowbridge, J. H. and Nowell, A. R. M. 1994. An introduction to the Sediment Transport Events on Shelves and Slopes (STRESS) program. *Cont. Shelf Res.* 14, 1057-1061.

Weatherly, G. L. 1972. A study of the bottom boundary layer of the Florida current. *J. Phys. Oceanogr.* 2, 54-72.

Weatherly, G. L. and Martin, P. J. 1978. On the structure and dynamics of the oceanic bottom boundary layer. *J. Phys. Oceanogr.* 8, 557-570.

White, M. 1994. Tidal and subtidal variability in the sloping benthic boundary layer. *J. Geophys. Res.* 99, 7851-7864.

Wiberg, P. L., Drake, D. E. and Cacchione, D. A. 1994. Sediment resuspension and bed armoring during high bottom stress events on the northern California inner continental shelf: measurements and predictions. *Cont. Shelf Res.* 14, 1191-1220.

Table 1: Statistics of the Terms in the Vertically Integrated Balances (SI Units)

Term	STRESS-1		STRESS-2	
	mean	std dev	mean	std dev
$-\rho_0 f \int_0^\delta (v - v_\delta) dz$	+0.0279	0.0338	+0.0315	0.0518
$-\tau_{bx}$	+0.0100	0.0198	+0.0149	0.0249
$\beta g[(\delta^2/2)(\partial T/\partial x) + \alpha \int_0^\delta (T - T_\delta) dz]$	+0.0113	0.0303	+0.0208	0.0549
$\rho_0(\partial/\partial t) \int_0^\delta (u - u_\delta) dz$	-0.0001	0.0051	+0.0001	0.0067
$\rho_0 f \int_0^\delta (u - u_\delta) dz$	-0.0114	0.0257	-0.0209	0.0321
$-\tau_{by}$	-0.0064	0.0305	-0.0124	0.0490
$\beta g(\delta^2/2)(\partial T/\partial y)$	-0.0039	0.0057	-0.0059	0.0070
$\rho_0(\partial/\partial t) \int_0^\delta (v - v_\delta) dz$	-0.0001	0.0060	+0.0001	0.0086
$10^4 \int_0^\delta (\partial T/\partial t) dz$	+0.1128	0.3417	+0.0676	0.5420
$-10^4(\partial T/\partial x) \int_0^\delta u dz$	+0.0641	0.2734	+0.1063	0.3632
$-10^4(\partial T/\partial y) \int_0^\delta v dz$	+0.1345	0.2704	+0.1580	0.3424
$\rho_0 f \int_0^h \overline{(u - u_h)} dz$	-0.0526	...	-0.0498	...
$-\overline{\tau}_{by}$	-0.0064	...	-0.0124	...
$\beta g(h^2/2)\overline{(\partial T/\partial y)}$	-0.0220	...	-0.0198	...

## Figure Captions

Figure 1. Configuration addressed in the theoretical development. A non-conducting sea floor is inclined at a locally uniform angle  $\alpha$  with respect to horizontal. A turbulent boundary layer adjacent to the sea floor is overlain by a stably stratified interior in which turbulent fluxes of momentum and heat are negligible.

Figure 2. STRESS study area on the northern California shelf. C3 is the central site and C2, C3' and C4 are secondary sites. C3 and C3' are at water depths of approximately 90 m and C4 is at a water depth of approximately 130 m. The coordinate system is oriented so that  $x$  is cross-isobath and  $y$  is along-isobath at C3.

Figure 3. STRESS instrumentation. During STRESS-1, the heights of the BASS sensors were 0.21, 0.51, 1.10, 1.96, 2.56 and 4.96 m; the heights of the temperature sensors were 0.37, 0.62, 1.10, 2.01, 2.51, 3.63, 5.00 and 5.84 m; and the heights of the VACMs were 6, 12, 18, 24 and 30 m at C3 and 6 and 18 m at C3'. During STRESS-2, the heights of the BASS sensors at C3 and C4 were 0.39, 0.74, 1.34, 1.94, 2.54 and 4.94 m; the heights of the temperature sensors were 0.19, 1.08, 1.75, 2.62, 3.76, 4.48, 5.14 and 5.83 m at C3 and 0.15, 2.93, 3.77, 4.53, 5.18, 5.96, 13, 23, 27, 41 and 56 m at C4; the heights of the temperature-conductivity sensors were 16, 22, 25 and 28 m at C3 and 7 m at C4; and the heights of the VACMs were 7, 10, 13, 19 and 31 m at C3 and 10, 19 and 71 m at C4. During STRESS-2, the third and sixth BASS above bottom at C3, the first and third BASS above bottom at C4, the second VACM velocity sensor above bottom at C3, and the lowest VACM conductivity sensor at C3 malfunctioned, as noted in the text. We do not use the highest STRESS-2 VACM record at C4, which, at 71 m above bottom, was far above the bottom mixed layer. Sensors above 35 m are not shown in the figure.

Figure 4. Temperature-density relationships based on hourly data at C3. The STRESS-1 mea-

measurements were obtained from temperature–conductivity sensors at heights of 6, 18 and 30 m above bottom. The STRESS-2 measurements were obtained from temperature–conductivity sensors at heights of 10, 13, 16, 19, 22, 25, 28 and 31 m. The solid lines represent least-squares fits to the temperature–density relationship, which correspond to  $\beta = 0.35 \text{ kg m}^{-3} \text{ deg}^{-1} \text{ C}$  for STRESS-1 and  $\beta = 0.29 \text{ kg m}^{-3} \text{ deg}^{-1} \text{ C}$  for STRESS-2.

Figure 5. Relationship between current speed, obtained from velocity averaged over the bottom three BASS sensors, and log-profile estimates of shear velocity for STRESS-1 (left panel) and STRESS-2 (right panel) based on the hourly data. The solid lines correspond to a quadratic drag law with a bottom roughness parameter of  $z_0 = 0.01 \text{ m}$ .

Figure 6. Rotary velocity spectra based on all functioning current sensors from STRESS-1 (top panel) and STRESS-2 (bottom panel). Positive and negative frequencies correspond to counter-clockwise and clockwise polarization, respectively. The inertial frequency is approximately -1.25 cpd. We estimated spectra by detrending and demeaning the data, applying a Hanning window, computing the discrete Fourier transform of the data in the complex form  $u + iv$ , squaring the absolute value of the Fourier coefficients, and averaging over 17 adjacent frequencies to obtain spectral estimates with 34 degrees of freedom. We obtained spectra for STRESS-1 by concatenating the time series for STRESS-1a and STRESS-1b. The more energetic spectra correspond to measurements higher in the water column.

Figure 7. Rotary spectra of bottom stress during STRESS-1 and STRESS-2, computed as in Figure 6.

Figure 8. Time series of filtered velocity and temperature during STRESS-1.

Figure 9. Time series of filtered velocity and temperature during STRESS-2.

Figure 10. Mean velocity and temperature together with EOF representation of filtered velocity and temperature fluctuations during STRESS-1 and SMILE (circles) and STRESS-2 (pluses). Measurements above 40 m are from the SMILE array.

Figure 11. Estimates of gradient Richardson number  $Ri$  at four heights based on hourly STRESS-1 measurements. The gradients are calculated based on differences between measurements at two different heights. The heights listed for  $Ri$  are the means of the heights of each pair of measurements. The pairs of heights are 18 and 12 m for the top panel, 12 and 6 m for the second panel, 4.96 and 2.56 m for the third panel, and 2.56 and 0.21 m for the fourth panel. Note that the vertical spacing between the pair of sensors is approximately 2.5 m for the bottom two panels and 6 m for the top two panels. The solid lines correspond to  $Ri = 1/4$ .

Figure 12. Terms in the cross-isobath momentum balance (9), estimated from the STRESS-1 measurements. For the top panel,  $r^2 = 0.17$ , and for the center panel,  $r^2 = 0.55$ . For convenience, the bottom panel shows the thickness of the bottom mixed layer.

Figure 13. Terms in the cross-isobath momentum balance (9), estimated from the STRESS-2 measurements. For the top panel,  $r^2 = 0.15$ , and for the center panel,  $r^2 = 0.54$ . For convenience, the bottom panel shows the thickness of the bottom mixed layer.

Figure 14. Terms in the along-isobath momentum balance (10), estimated from the STRESS-1 measurements. For the top panel,  $r^2 = 0.33$ , and for the bottom panel,  $r^2 = 0.33$ .

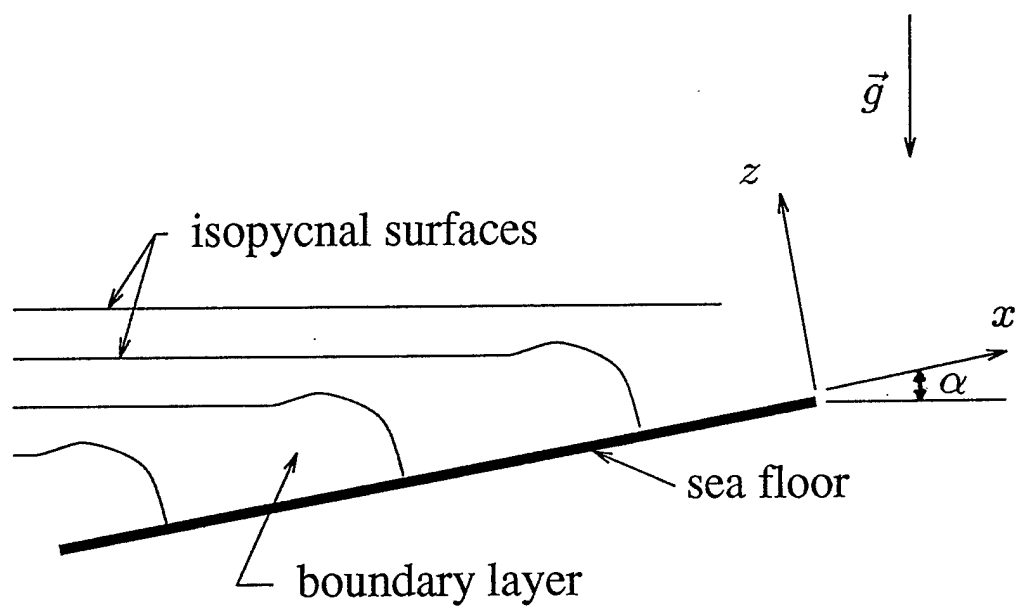
Figure 15. Terms in the along-isobath momentum balance (10), estimated from the STRESS-2 measurements. For the top panel,  $r^2 = 0.26$ , and for the bottom panel,  $r^2 = 0.34$ .

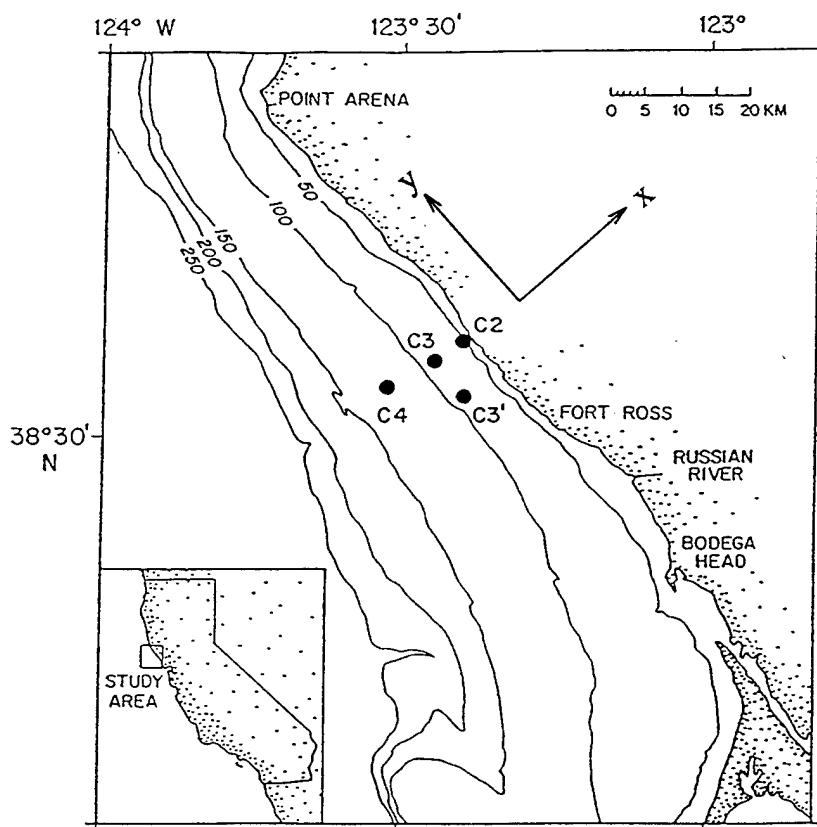
Figure 16. Terms in the integrated heat balance (11), estimated from the STRESS-1 measurements. For the top panel,  $r^2 = 0.11$ , and for the bottom panel,  $r^2 = 0.35$ .

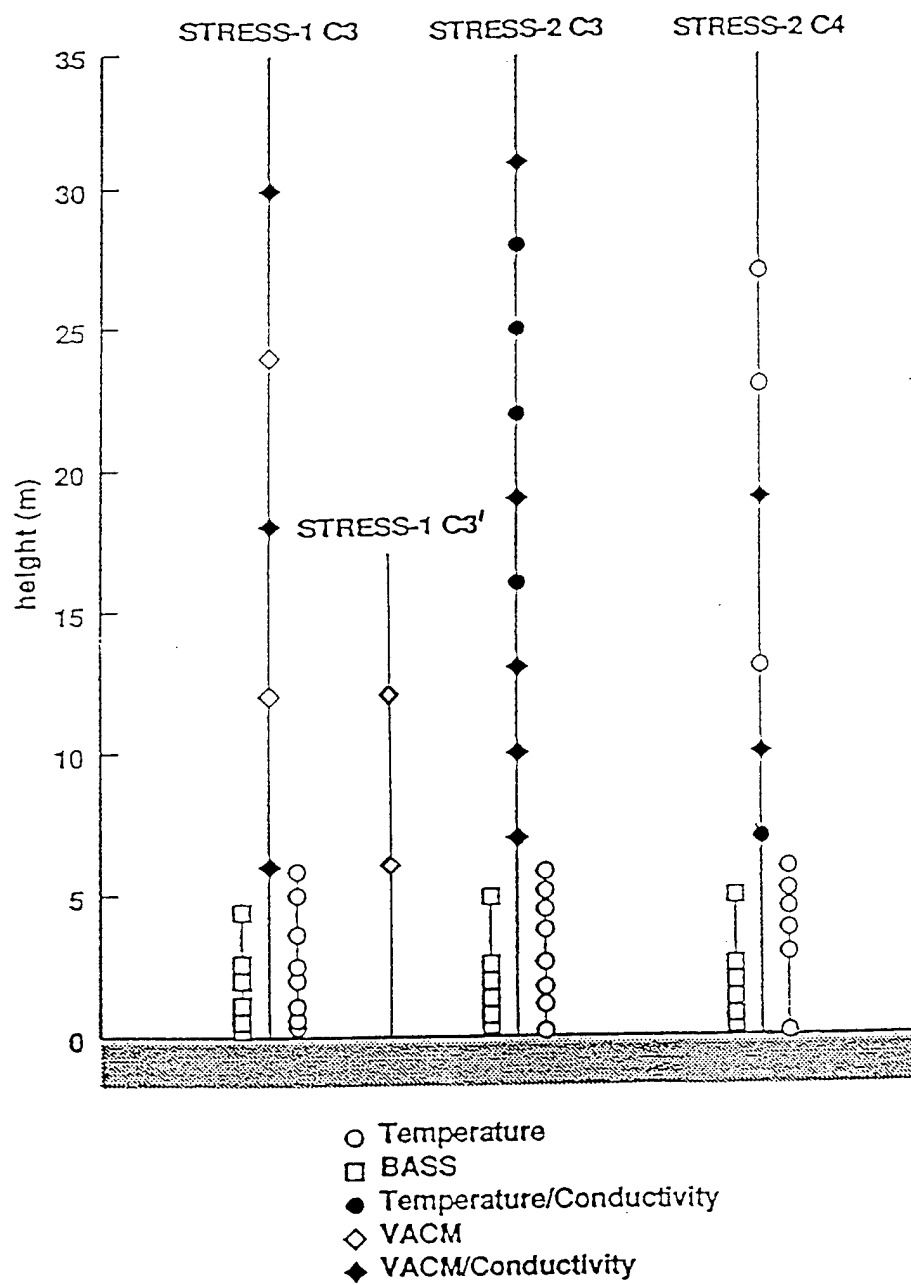
Figure 17. Terms in the integrated heat balance (11), estimated from the STRESS-2 measurements. For the top panel,  $r^2 = 0.27$ , and for the bottom panel,  $r^2 = 0.50$ .

Figure 18. Mean velocity and temperature profiles for upwelling event near day 10 during STRESS-1 (January 10, 1989).

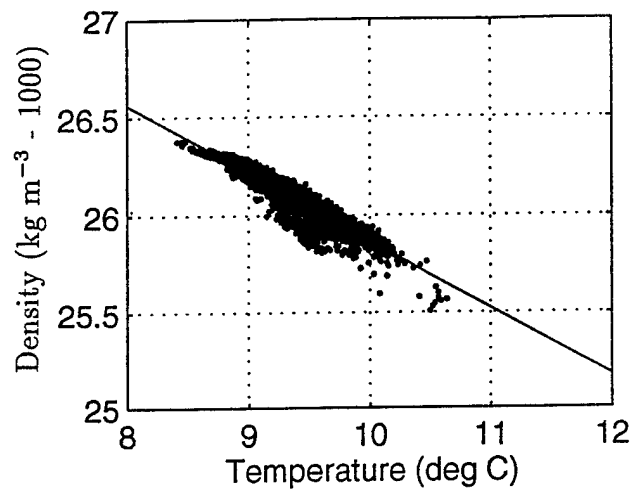




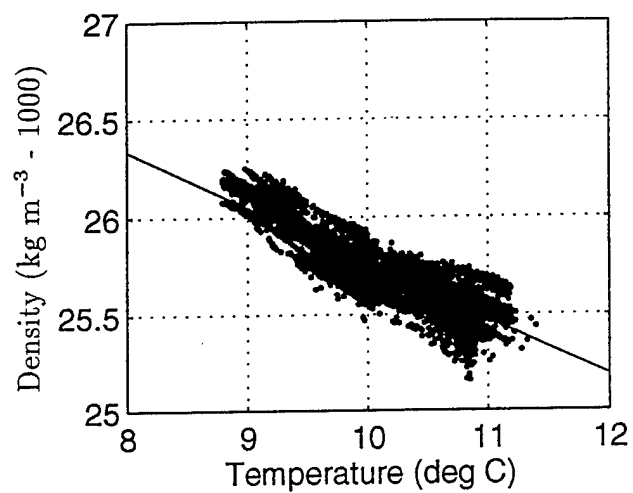


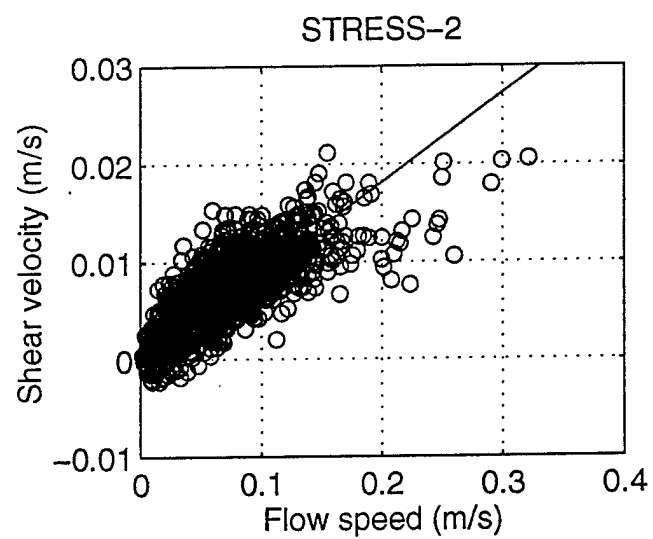
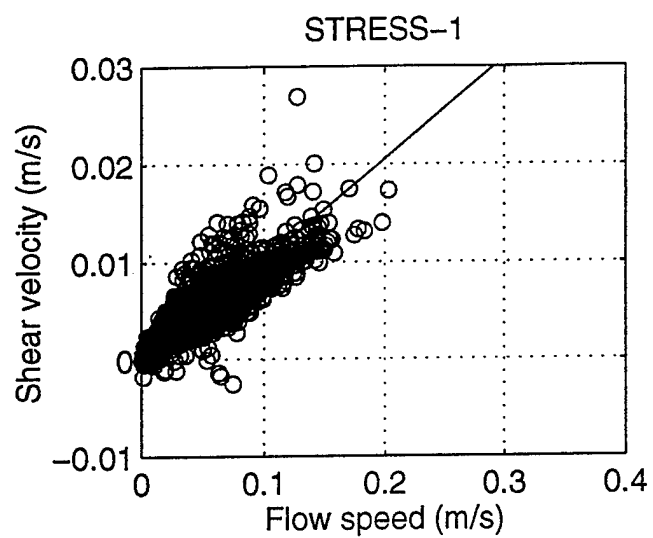


STRESS-1

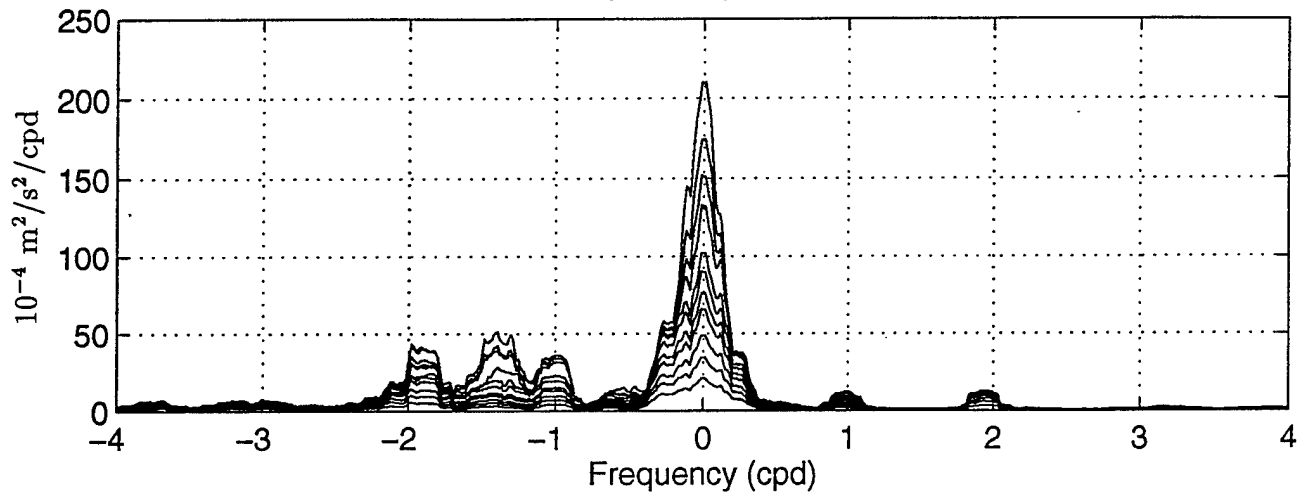


STRESS-2

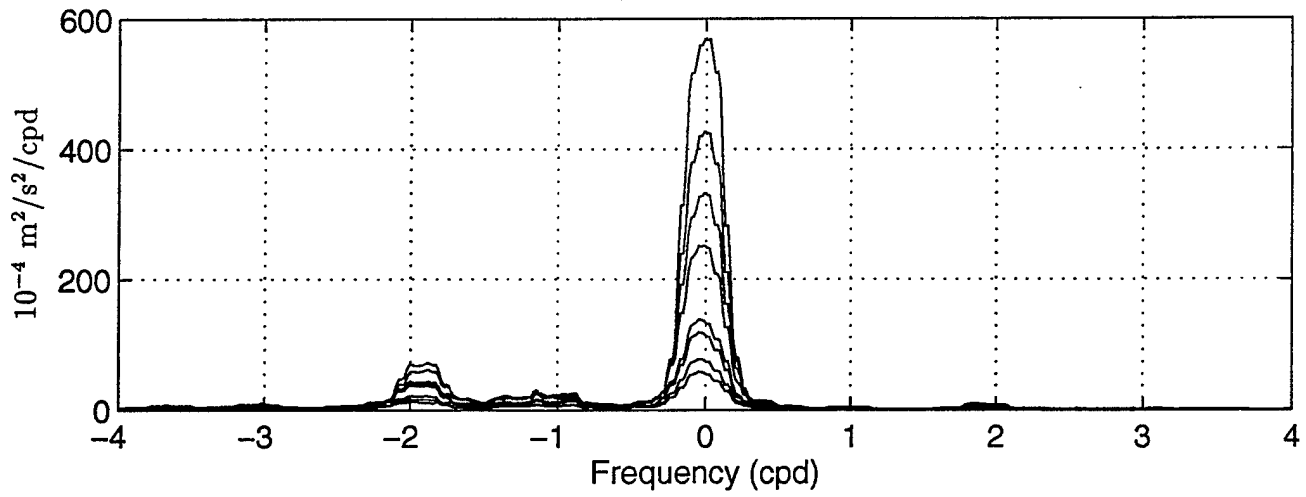




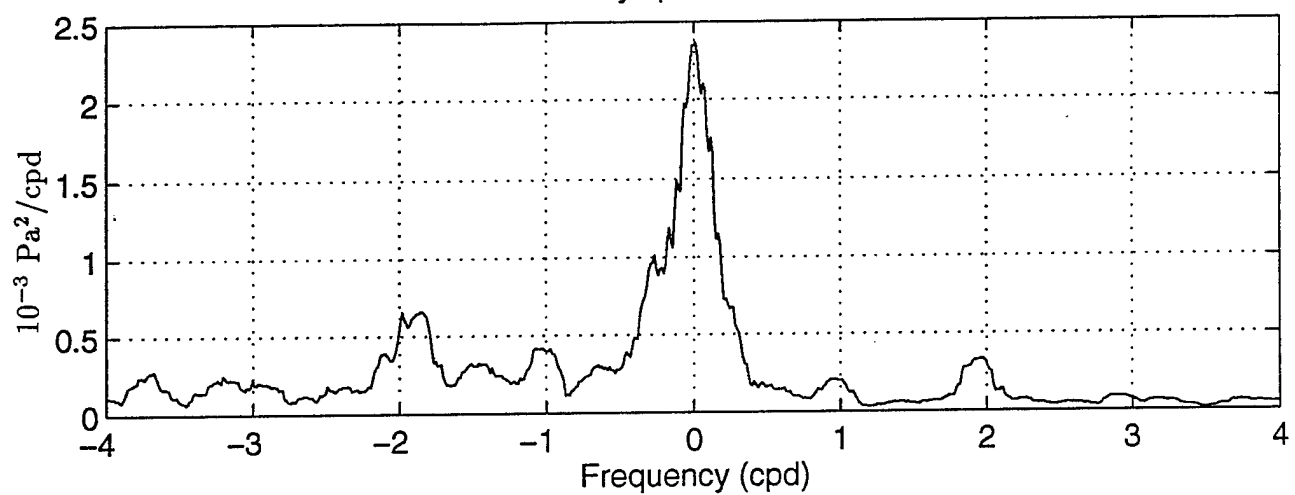
STRESS-1 rotary velocity spectra at 11 heights



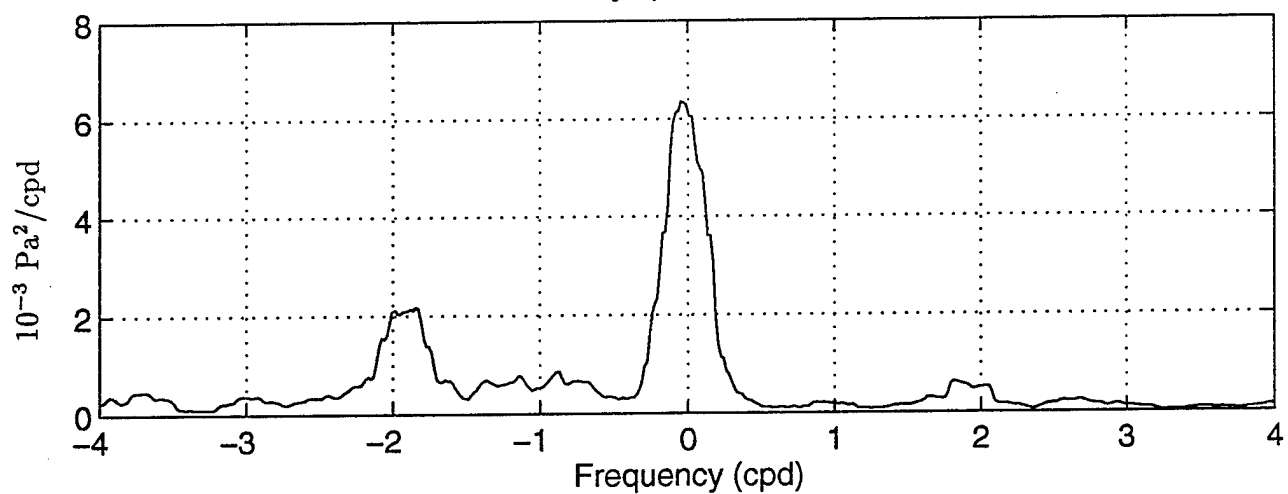
STRESS-2 rotary velocity spectra at 8 heights



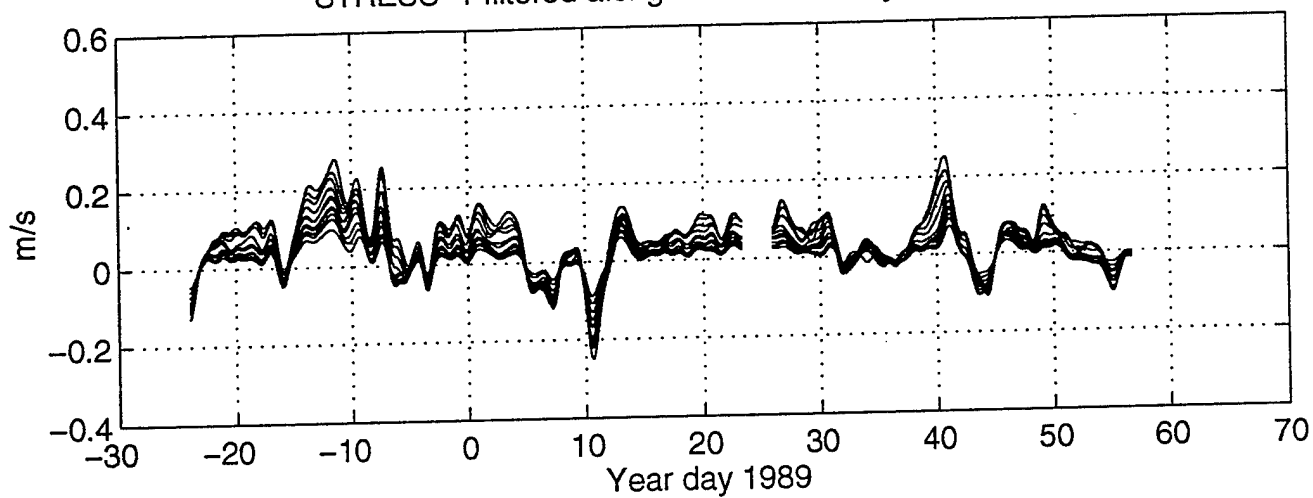
STRESS-1 rotary spectrum of bottom stress



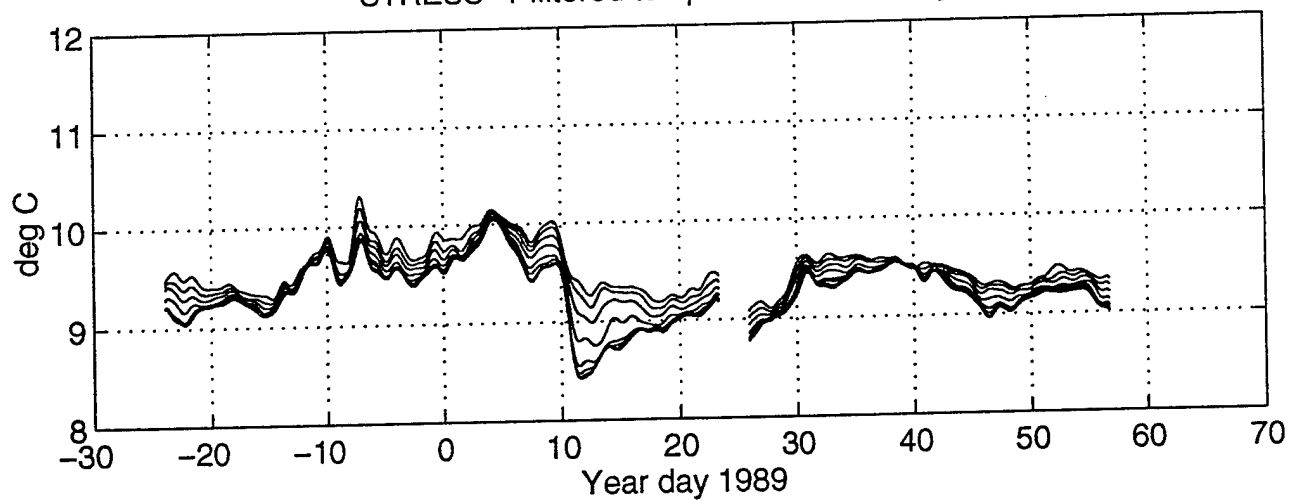
STRESS-2 rotary spectrum of bottom stress



STRESS-1 filtered along-isobath velocity at 11 heights

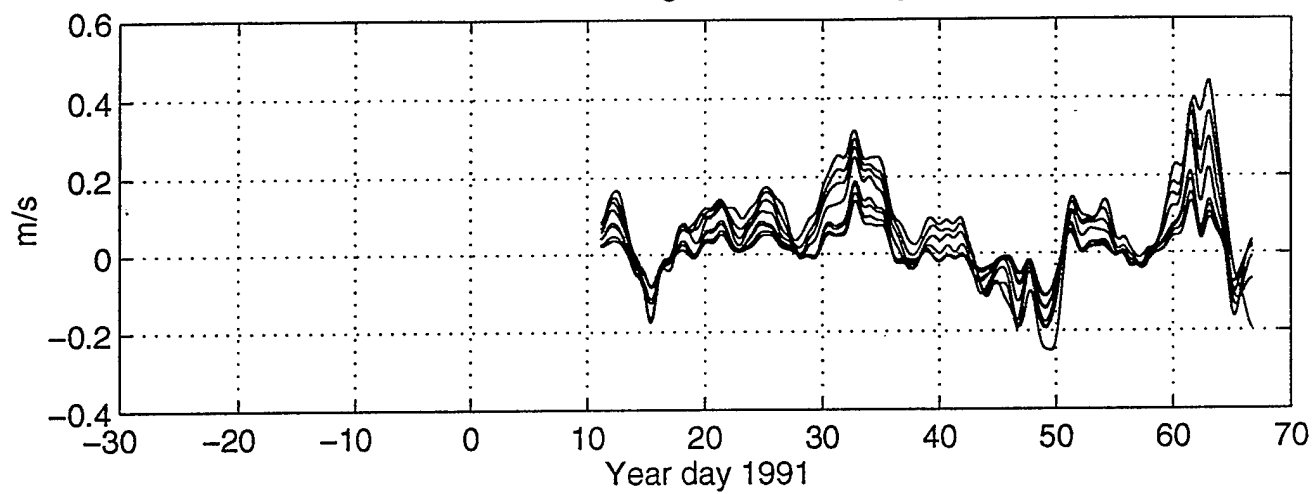


STRESS-1 filtered temperature at 11 heights

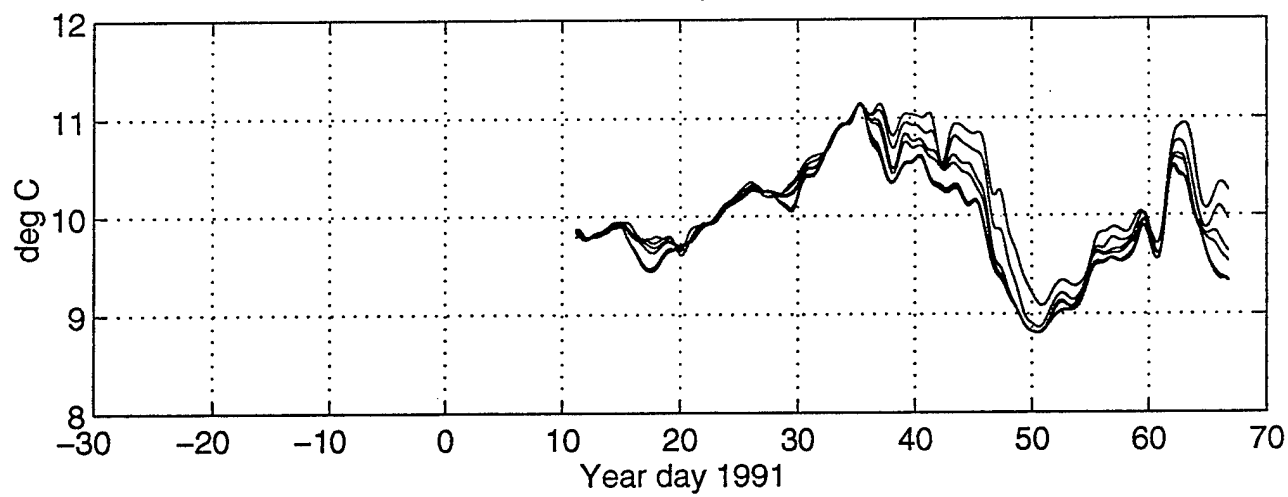


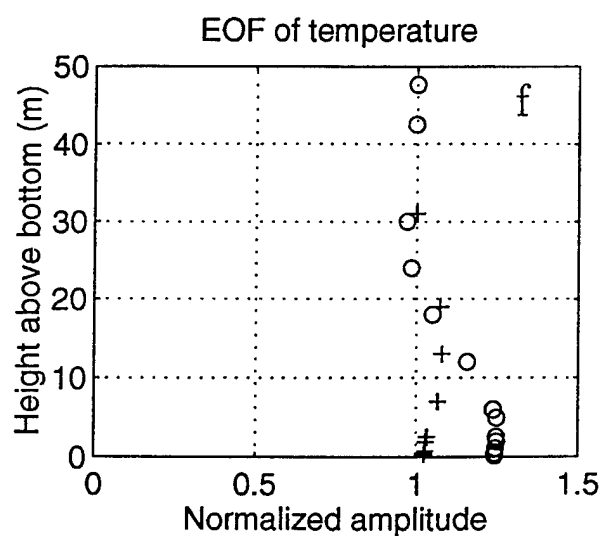
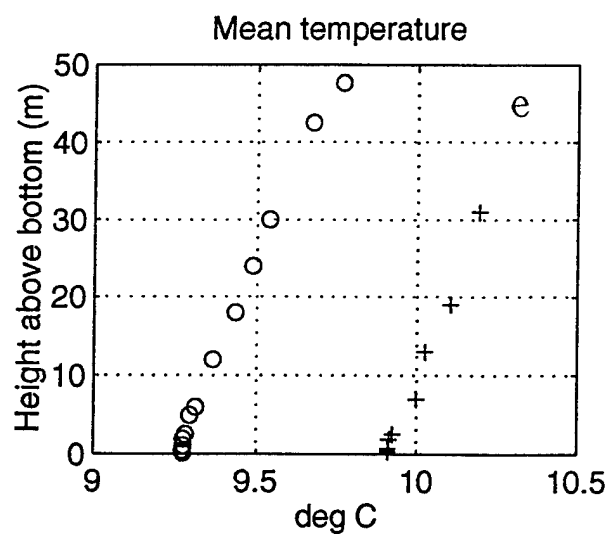
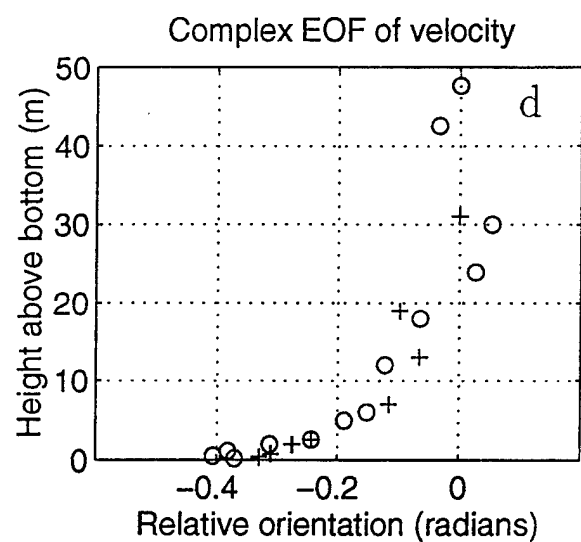
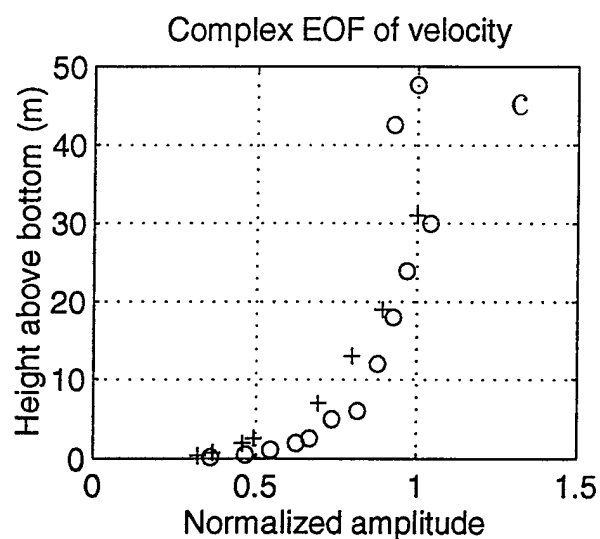
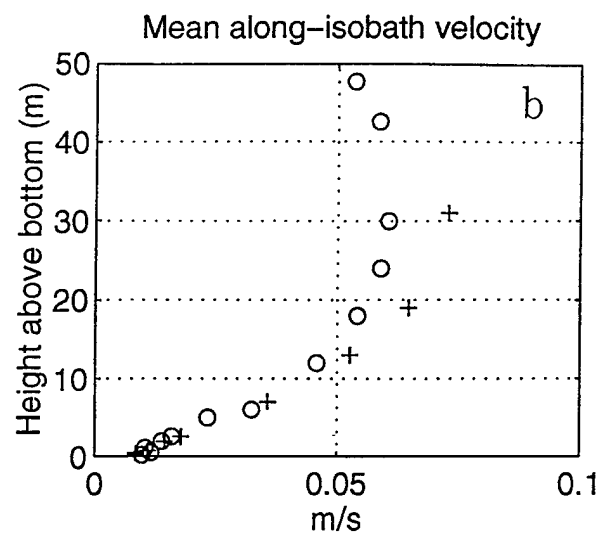
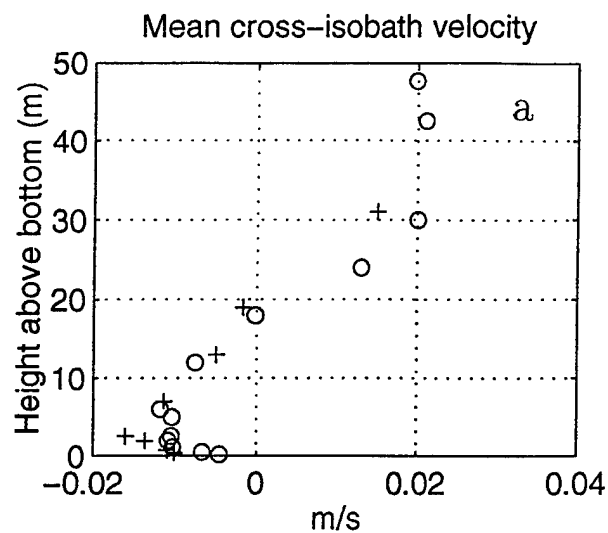


STRESS-2 filtered along-isobath velocity at 8 heights

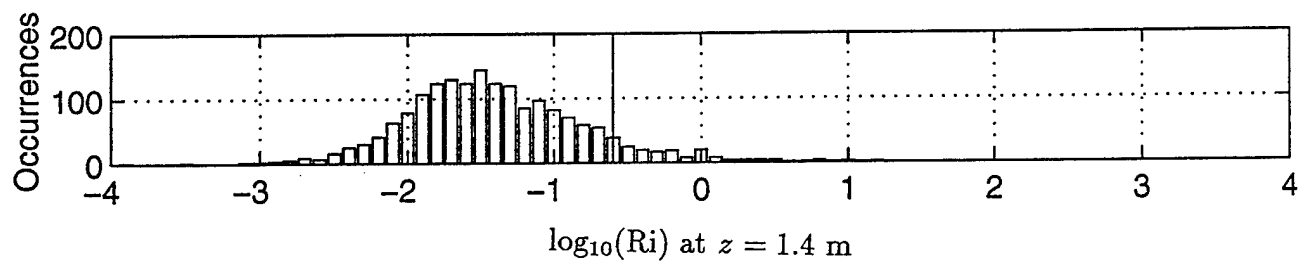
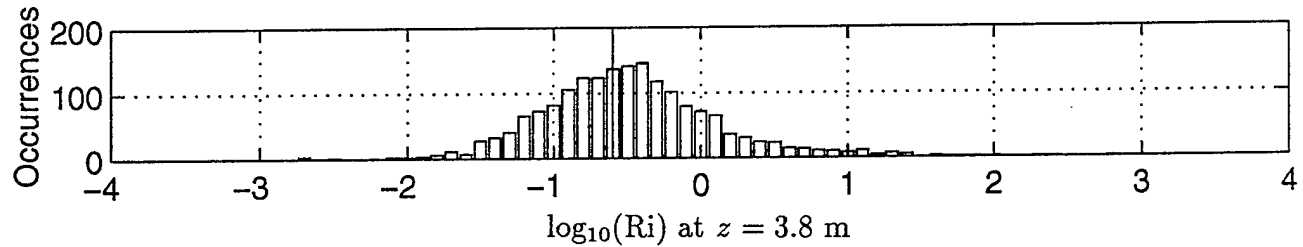
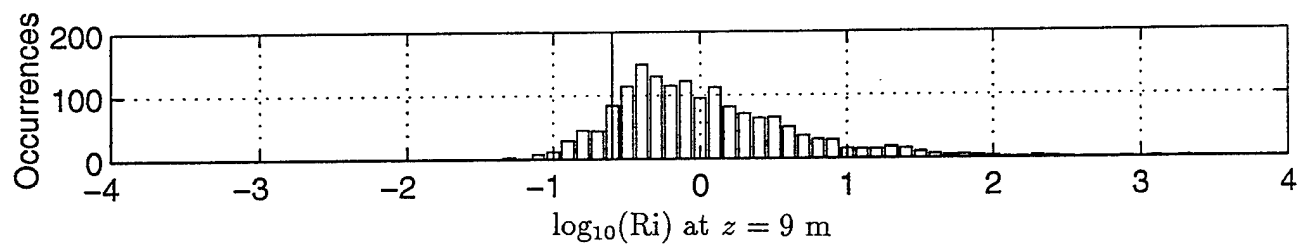
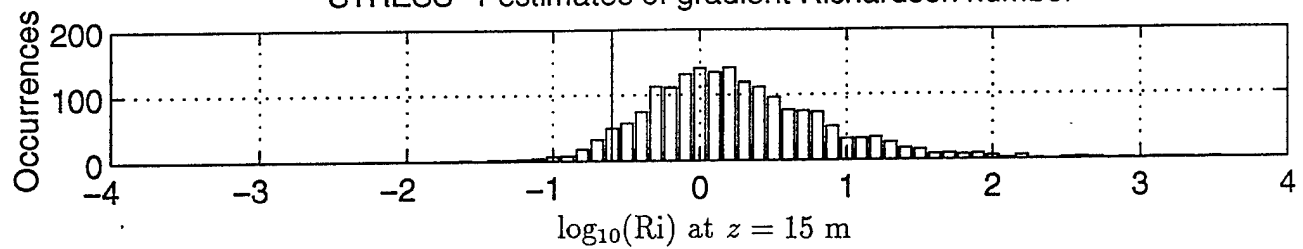


STRESS-2 filtered temperature at 8 heights

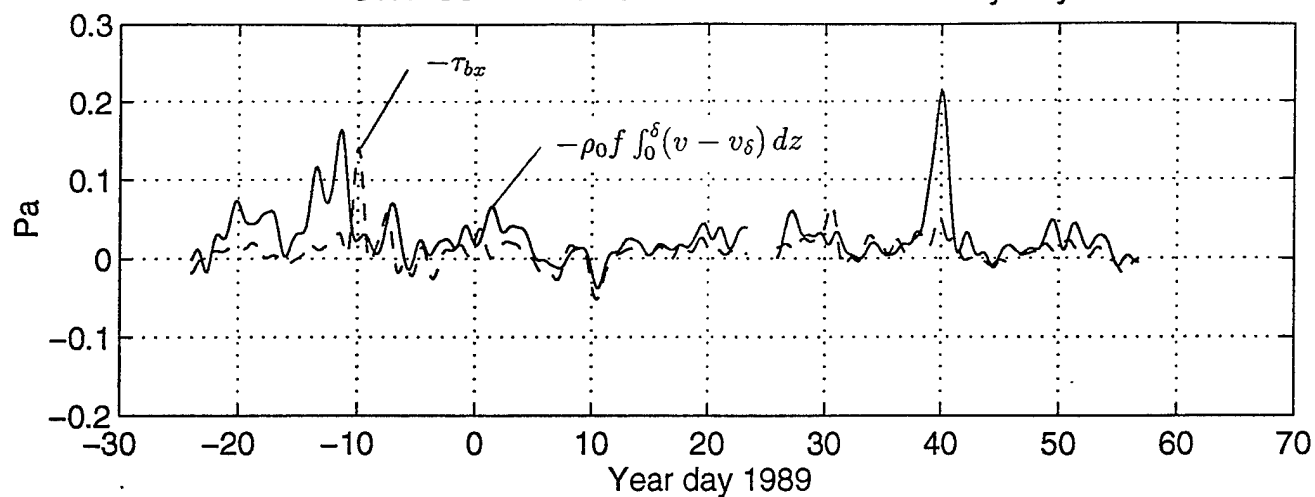




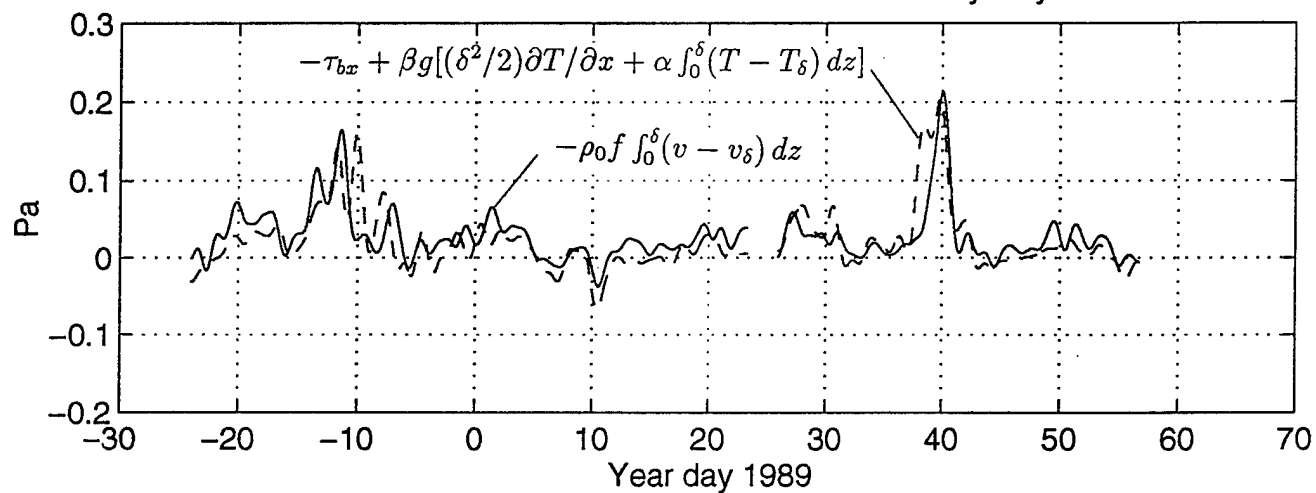
STRESS-1 estimates of gradient Richardson number



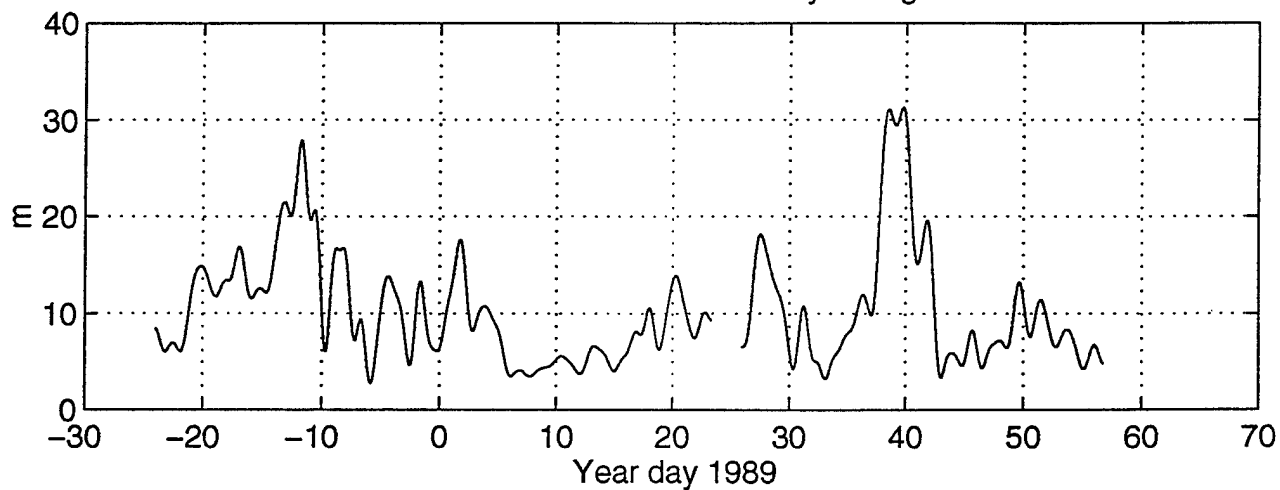
STRESS-1 x momentum balance without buoyancy



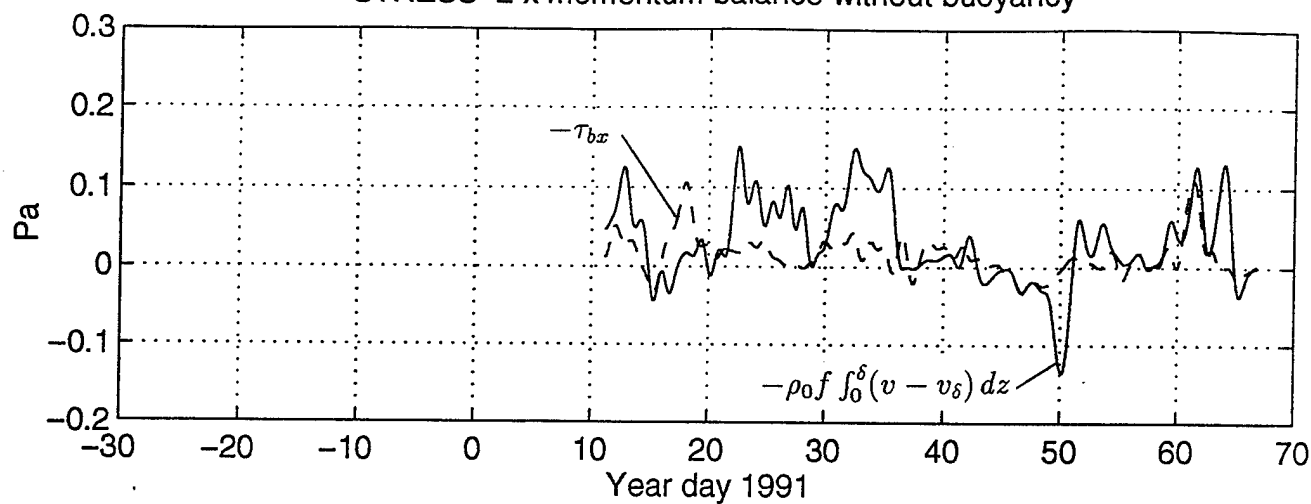
STRESS-1 x momentum balance with buoyancy



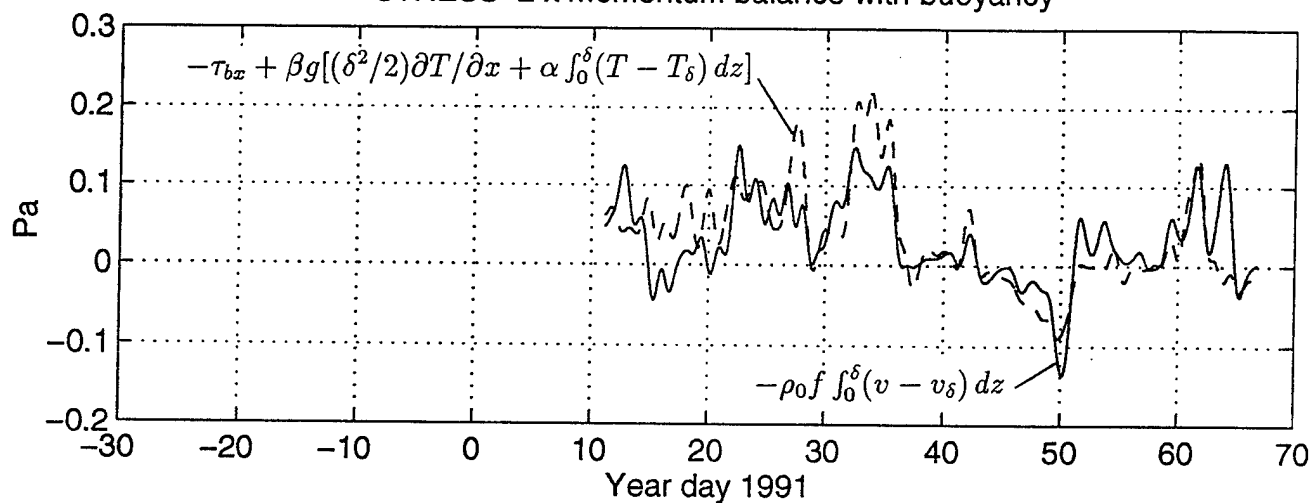
STRESS-1 filtered mixed-layer height



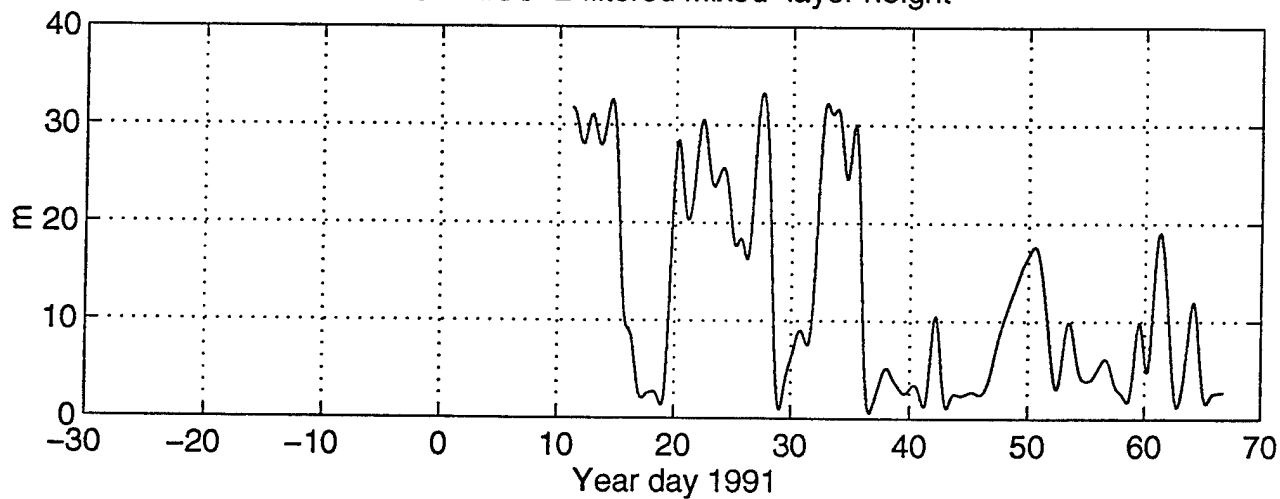
STRESS-2 x momentum balance without buoyancy



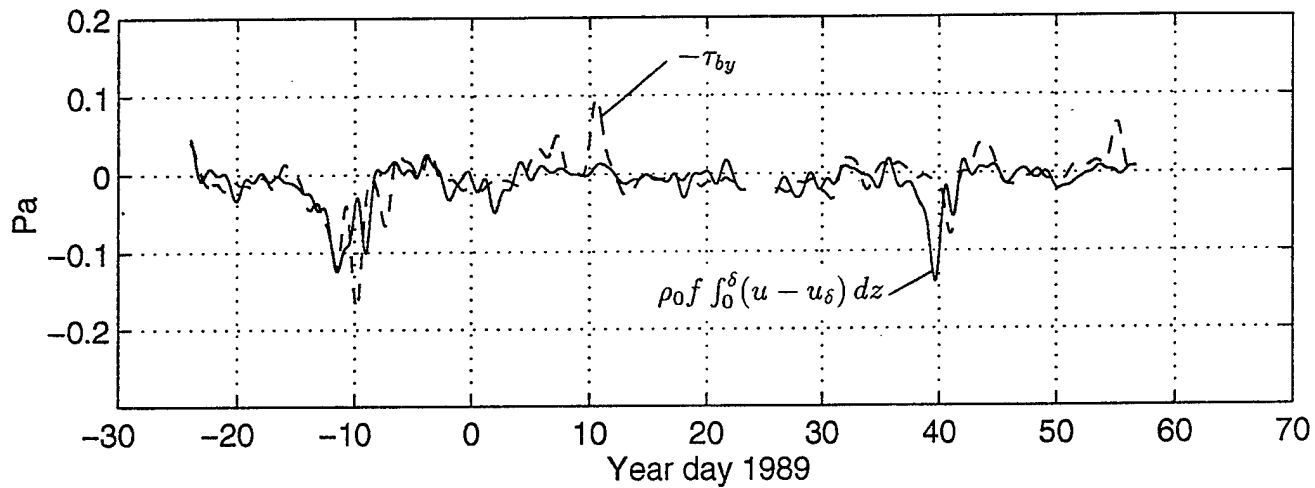
STRESS-2 x momentum balance with buoyancy



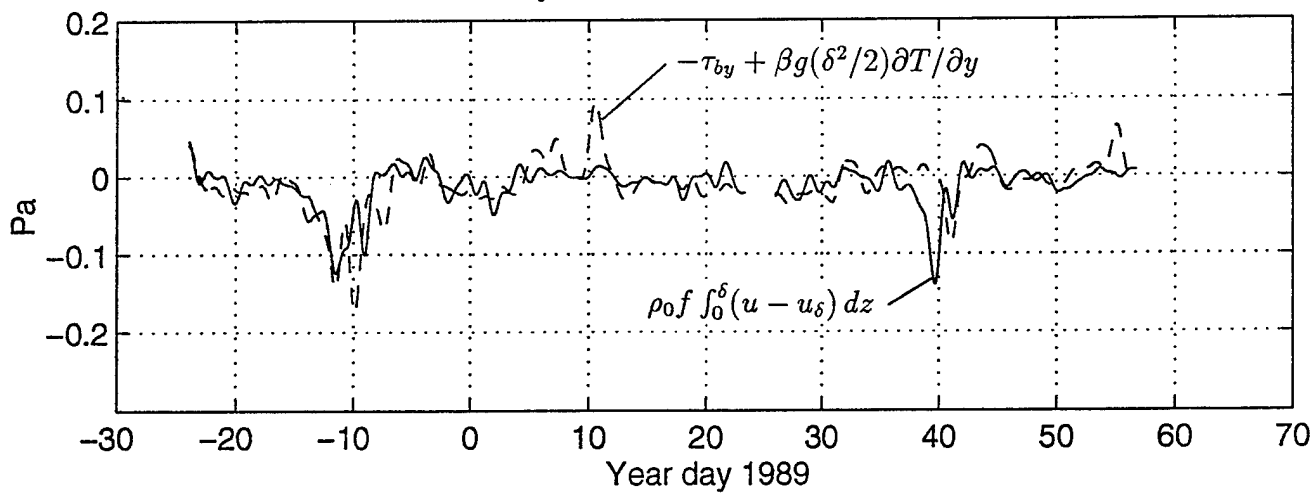
STRESS-2 filtered mixed-layer height



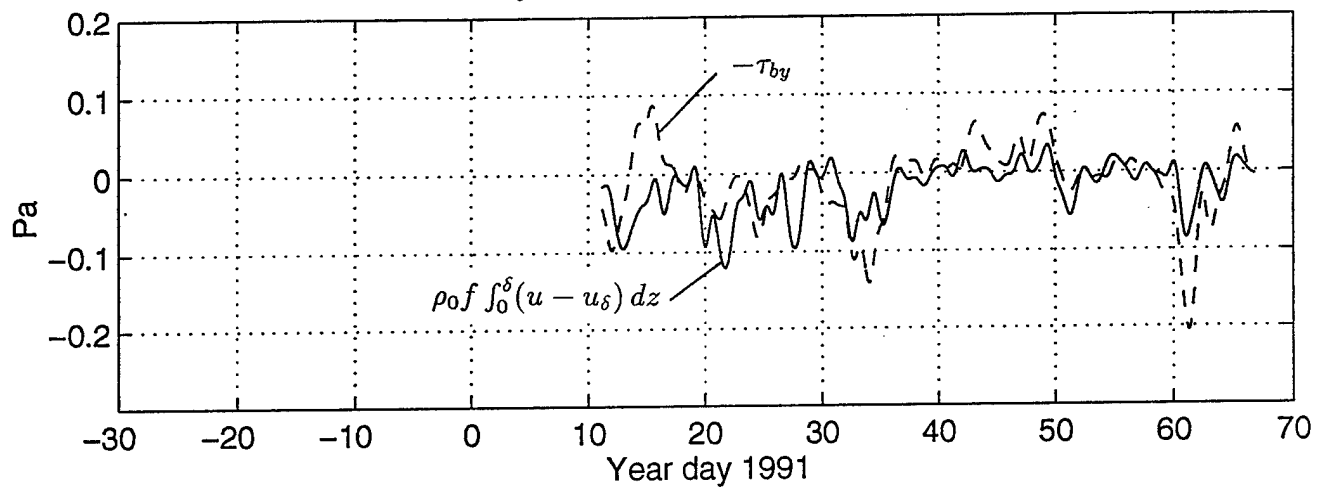
STRESS-1 y momentum balance without buoyancy



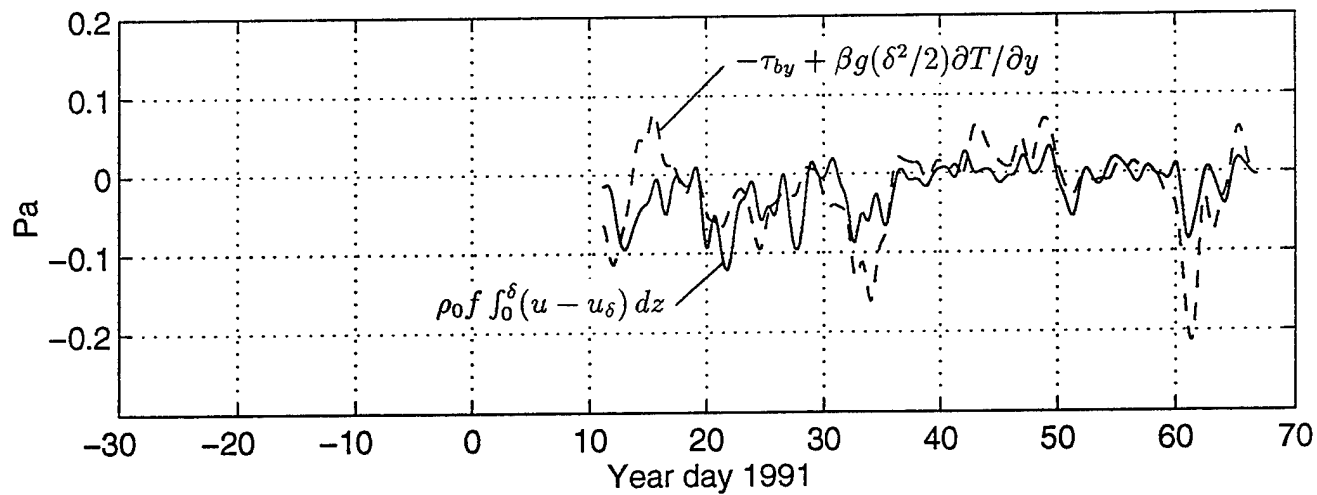
STRESS-1 y momentum balance with buoyancy



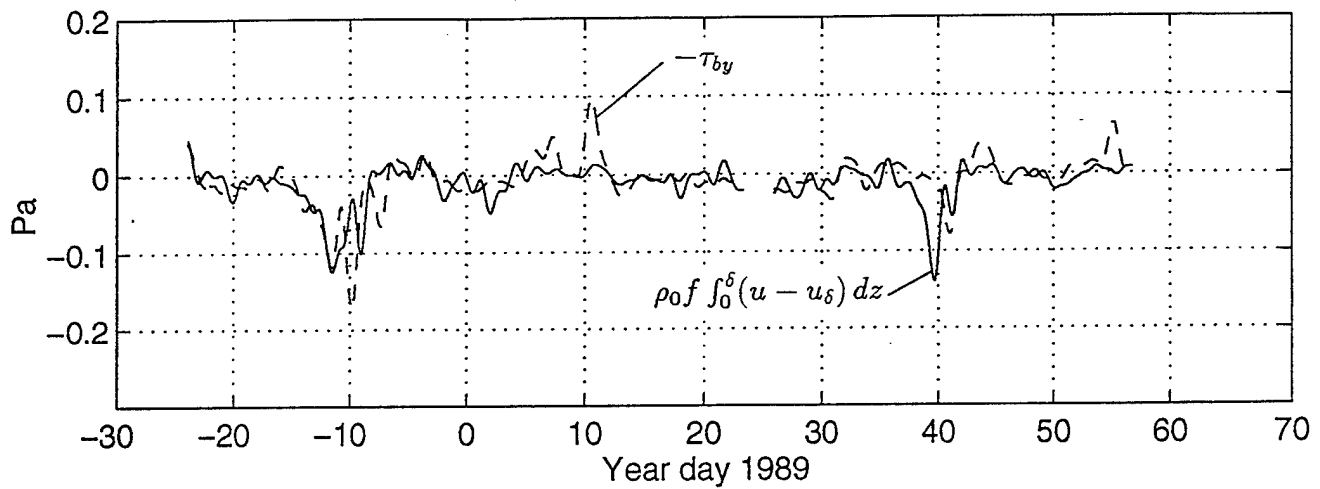
STRESS-2 y momentum balance without buoyancy



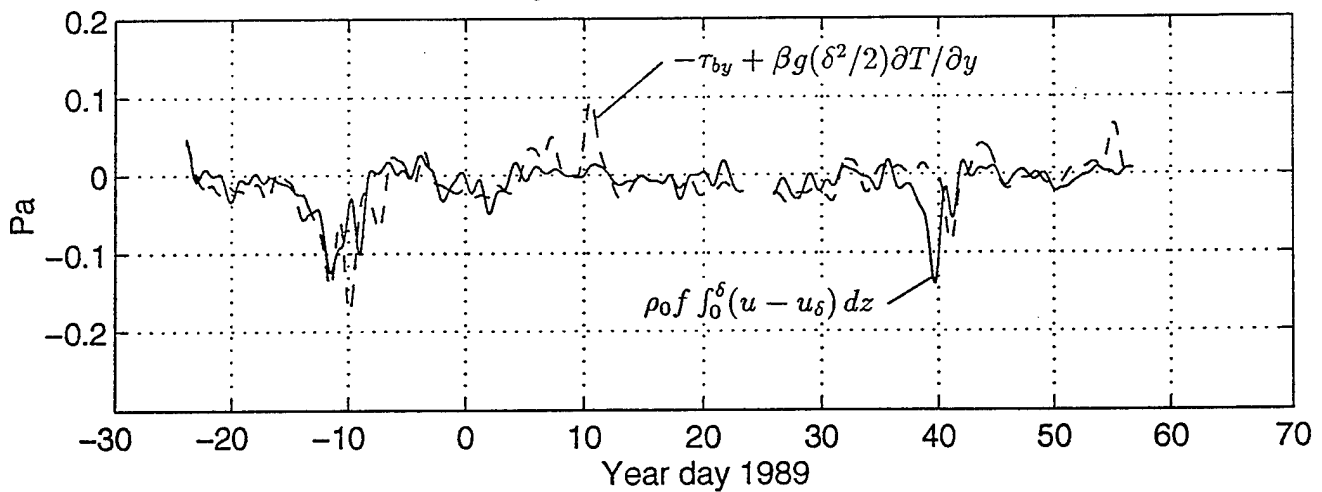
STRESS-2 y momentum balance with buoyancy



STRESS-1 y momentum balance without buoyancy

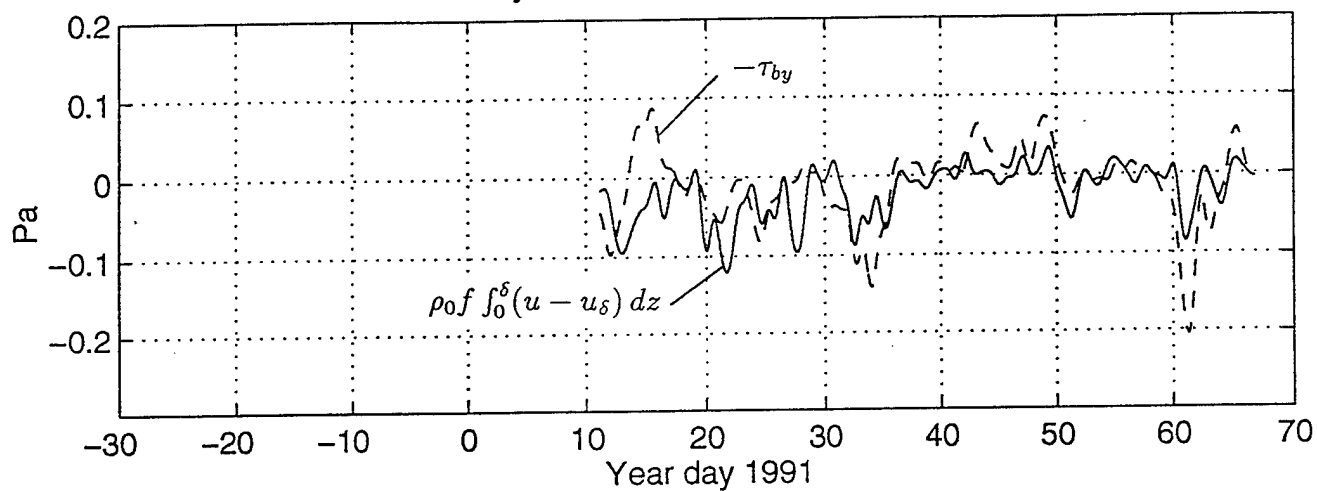


STRESS-1 y momentum balance with buoyancy

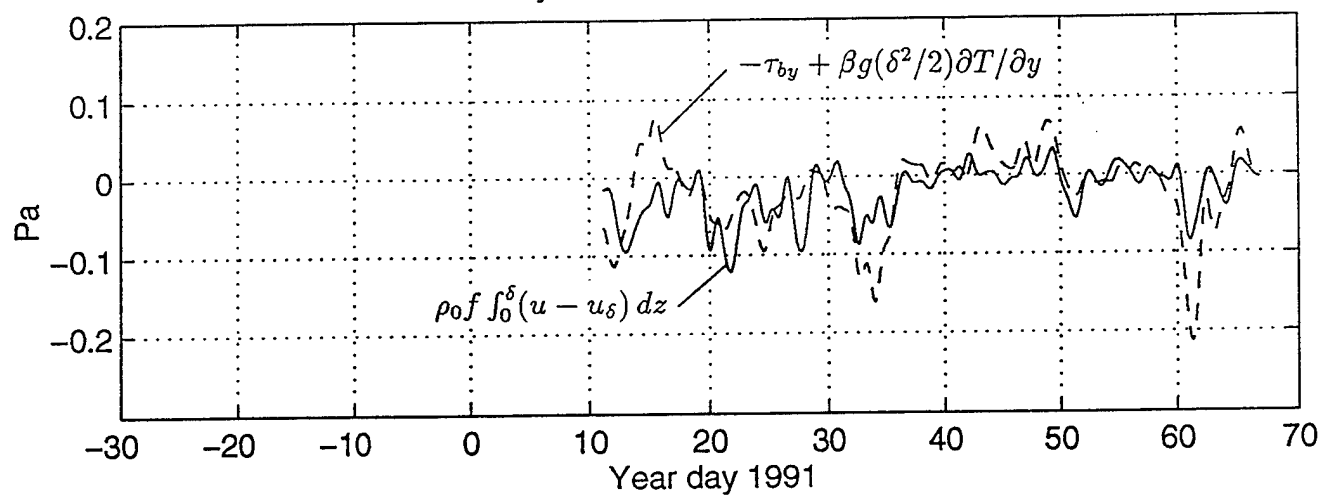




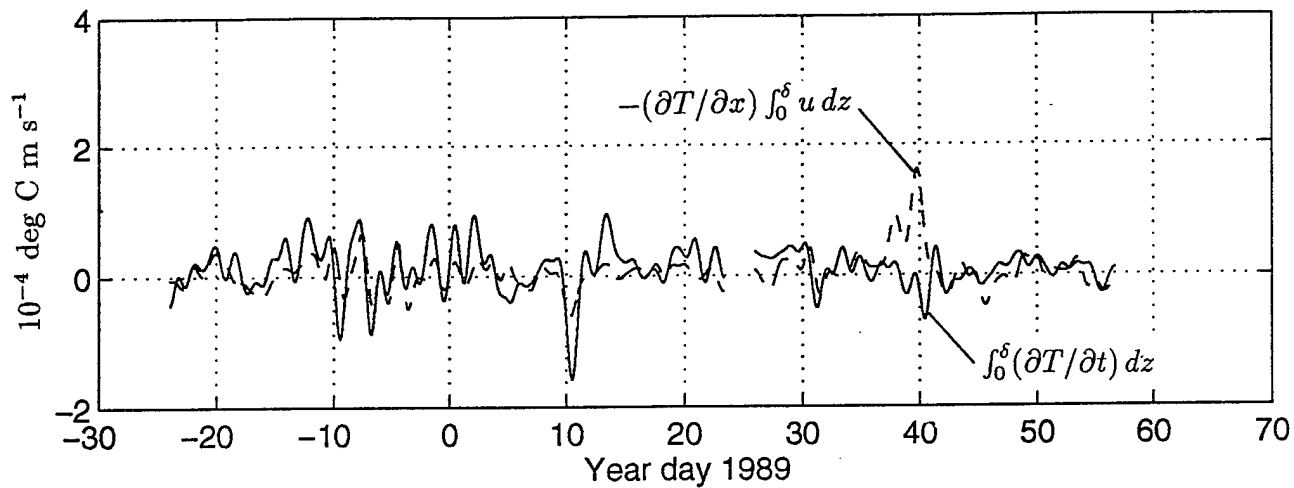
STRESS-2 y momentum balance without buoyancy



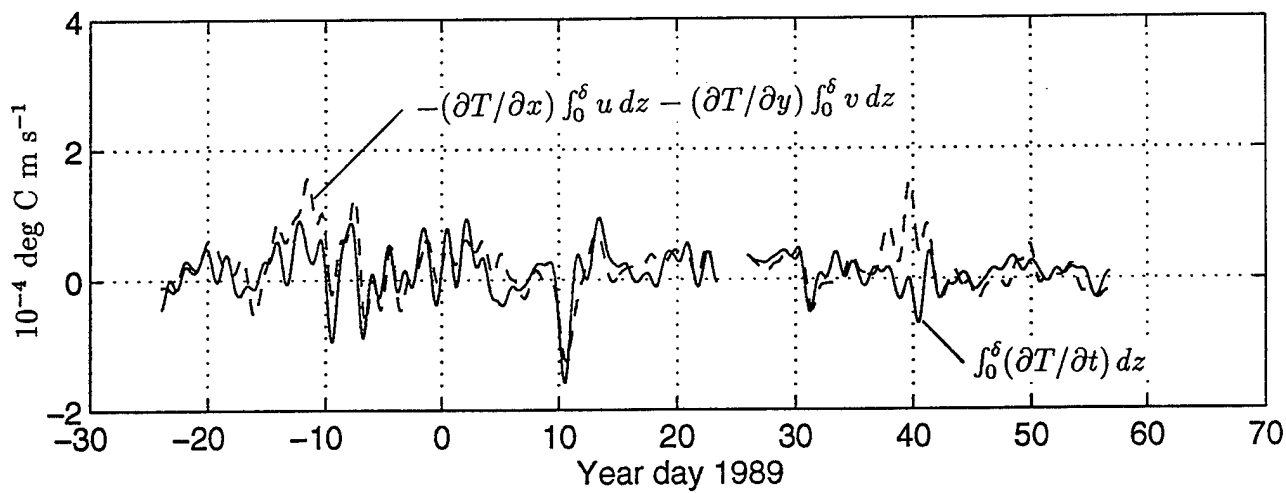
STRESS-2 y momentum balance with buoyancy



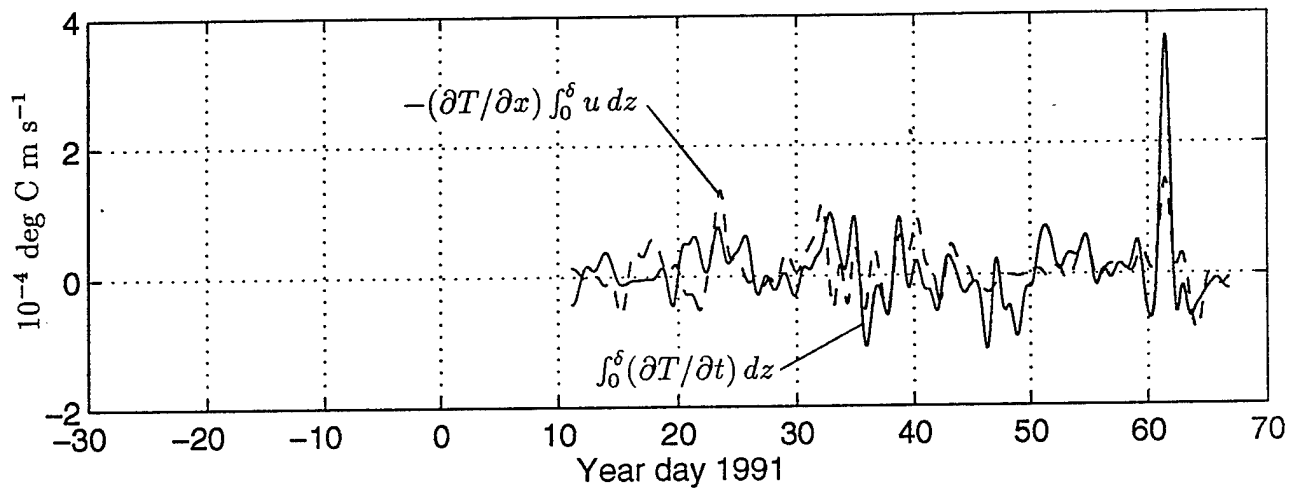
STRESS-1 heat balance without along-isobath advection



STRESS-1 heat balance with along-isobath advection



STRESS-2 heat balance without along-isobath advection



STRESS-2 heat balance with along-isobath advection

